Simple framework for systematic high-fidelity gate operations

Maximilian Rimbach-Russ, Stephan G.J. Philips, Xiao Xue, and Lieven M.K. Vandersypen
QuTech and Kavli Institute of Nanoscience, Delft University of Technology, Lorentzweg 1, 2628 CJ Delft, The Netherlands

arXiv:2211.16241v1 [quant-ph] 29 Nov 2022

Semiconductor spin qubits demonstrated single-qubit gates with fidelities up to 99.9% benchmarked in the single-qubit subspace. However, tomographic characterizations reveals non-negligible crosstalk errors in a larger space. Additionally, it was long thought that the two-qubit gate performance is limited by charge noise which couples to the qubits via the exchange interaction. Here, we show that coherent error sources such as a limited bandwidth of the control signals, diabaticity errors, microwave crosstalk, and non-linear transfer functions can equally limit the fidelity. We report a simple theoretical framework for pulse optimization that relates erroneous dynamics to spectral concentration problems and allows for the reuse of existing signal shaping methods on a larger set of gate operations. We apply this framework to common gate operations for spin qubits and show that simple pulse shaping techniques can significantly improve the performance of these gate operations in the presence of such coherent error sources. The methods presented in the paper were used to demonstrate two-qubit gate fidelities with $F > 99.5\%$ in Ref. [Xue et al, Nature **601**, 343]. We also find that single and two-qubit gates can be optimized using the same pulse shape. We use analytic derivations and numerical simulations to arrive at predicted gate fidelities greater than 99.9% with duration less than $4/(\Delta f)$ where Δf is the difference in qubit frequencies.

I. INTRODUCTION

Spin qubits based on electrons confined in quantum dots (QDs) [1] are a leading candidate for long-term applications in quantum information processing. They provide long relaxation times [2–12] and their lithographic fabrications allow for dense and scalable qubit architectures [13, 14]. Using isotopically enriched silicon (Si) [15] or germanium (Ge) [16] in favor of gallium arsenide (GaAs) [1] as the host material for the quantum dots allows for significant longer decoherence times due to the low abundance of nuclear spins. One common feature of all spin qubits is the need for electric control on the nanoscale which typically also couples the system to electrical noise.

Depending on the host material single-qubit gates are either implemented using electron spin resonance (ESR) [17–19] or electric-dipole spin resonance (EDSR) [20–25] by applying microwave signals at the qubit resonance frequency.

On the other hand, all-electrical two-qubit gates can be implemented using dc gate voltage pulses that switch on and off the exchange interaction [26]. However, the originally proposed universal $\sqrt{\text{SWAP}}$ gate [26] was found to be unpractical to yield high fidelities in the case finite differences in qubit frequencies [27, 28] are introduced for qubit addressability [13] and strong dephasing from charge noise in the regime $100\,\text{MHz} < J < 10\,\text{GHz}$ [10, 29, 30]. In the presence of a finite difference in qubit frequencies, the adiabatic CZ gate, where a conditional phase difference is acquired by an adiabatic exchange pulse, is less stringent to hardware at the cost of longer gate times [28]. Two-qubit gates with fidelities $F > 99\%$ [31–34] were recently reported with highest fidelities achieved by the adiabatic CZ gate [31, 34].

Even without the presence of decoherence, qubit operations can be subject to errors. These coherent errors can arise from miss-calibration, crosstalk, non-adiabicity, finite bandwidths, filtered signals, non-linear transfer functions, from certain approximations made such as the rotating wave approximation, and many other spectator and control errors [13]. Depending on the specifics, coherent errors can easily be larger than those from decoherence.

The standard approach for mitigating these errors is summarized in optimal control theory [35] which can be divided into three main approaches. Firstly, a geometric approach that rewrites the time evolution into Pontryagin's Maximum Principle [36]. The optimal control pulse is then given by the extreme conditions that satisfy the given boundary conditions. However, analytical solutions are mostly limited to small and simple systems. Secondly, fully numerical techniques, such as the GRAPE [37] and CRAB algorithms [38], can be used to find a (hopefully) global minima of the error by varying parameters of the input signal. This comes at the cost of speed and flexibility to small modifications. Lastly, inherent error mitigation can be achieved via (enforced) adiabatic dynamics [39–42].

In this paper we want to provide a simple framework to reduce coherent errors based on the adiabatic approach. We start in Section II by introducing a framework which allows us to separate the desired dynamics which is the target gate from erroneous dynamics that yields gate errors. We also show how existing methods from literature [40–42] are captured within this framework and can be reapplied to a larger set of gate operations. We then apply this framework in section III to derive optimized pulse shapes that reduce the errors on the most widly used single- and two-qubit gates for spin qubits. Subsequently in section IV, we numerically demonstrate the effectiveness of the derived pulse shapes in the presence of incoherent noise sources and benchmark them via the average gate fidelity [43]. By significantly reducing the magnitude of coherent errors our simulations show that gate fidelities $F > 99.9\%$ with duration less than 50 ns are feasible.

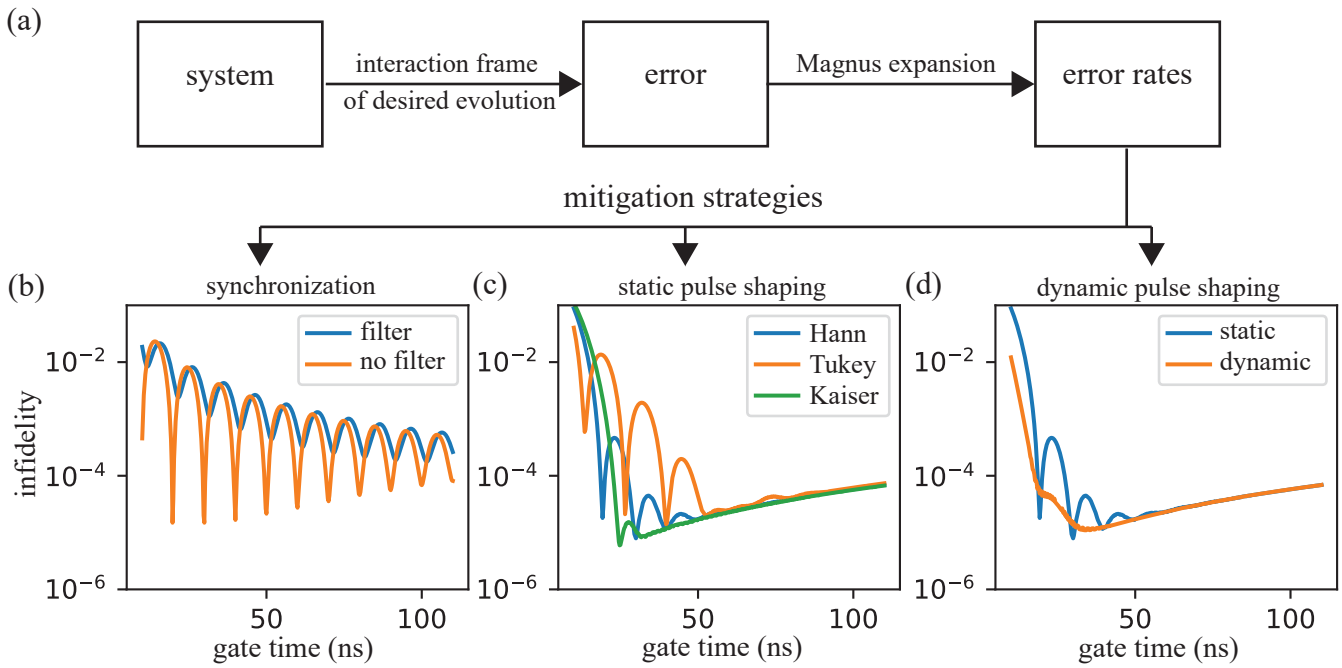

FIG. 1. (a) Flowchart of the proposed framework for error mitigation. The system Hamiltonian $H = H_{\text{ideal}} + H_{\text{rest}}$ is separated into an ideal part covering the dominant interaction and a small erroneous part consisting of imperfections. After transforming into the interaction frame with respect to H_{ideal} a Magnus expansion is performed to compute the error rates. (b)-(d) Mitigation strategies to reduce coherent errors shown for the example of a single-qubit $R_x(\pi/2)$ gate in a double-dot system with qubit frequency difference $\Delta E_z = 100\,\text{MHz}$. (b) Simulated infidelity of the gate operation as a function of the pulse-length with a control Hamiltonian that is instantanly turned on and off with (blue) and without (orange) filtering. Minima correspond to the synchronization condition (see Refs. [44, 45]). (c) Simulated infidelity of the gate operation as a function of the pulse-length for different filtered pulse shapes optimized to concentrate the energy spectral density [46]. (d) Simulated infidelity of the gate operation as a function of the pulse-length using a filtered Hann window with (blue) and without (orange) additional dynamic pulse shaping [40]. Simulation parameters are discussed in Appendix E. No incoherent noise sources are included. The gradual increase in infidelity for longer gate times is due to a residual exchange interaction between the qubits of 60 kHz.

II. FRAMEWORK FOR OPTIMIZING PULSE SHAPES

Fig. 1 displays our general framework for finding optimized pulse shapes to mitigate coherent errors. We start considering a quantum system with a Hilbert space $\mathcal{H}$ which is described by a Hamiltonian H of dimension $n \times n$. Ignoring any incoherent dynamics, the time-evolution from $t = 0$ to a final time $t = t_g$ generated by a Hamiltonian is given by

$$U = \mathcal{T} \exp\left(-\frac{i}{\hbar}\int_0^{t_g} H(t')dt'\right), \tag{1}$$

where $\mathcal{T}\exp$ is the usual time-ordering operator. We imply that U describes an operation which is close to an ideal or a targeted operation described by the unitary operation U_{ideal}. We can now define the erroneous operation as

$$\mathcal{E} = U_{\text{ideal}}^{\dagger} U. \tag{2}$$

The standard approach of estimating the errors is by measuring the average gate fidelity of the erroneous operation

$$F = \frac{|\text{tr}(\mathcal{E})|^2 + d}{d(d+1)}, \tag{3}$$

where d is the dimension of the Hilbert space. For a noisy process described by a superoperator χ we replace $|\text{tr}(\mathcal{E})|^2 \to \text{tr}(\chi)$ in Eq. (3). There are two standard approaches to experimentally access the gate fidelity, process tomography [47] and randomized benchmarking [48], both requiring complex circuits and analysis and either susceptible to state preparation and measurement (SPAM) errors or limited in the information gain. However, much progress is made to increase the information gain and reduce the susceptibility to SPAM errors [49, 50].

In order to estimate the errors, we separate $H = H_{\text{ideal}} + H_{\text{rest}}$ where H_{ideal} is defined as generating the targeted gate

$$U_{\text{ideal}} = \mathcal{T} \exp\left(-\frac{i}{\hbar}\int_0^{t_g} H_{\text{ideal}}(t')dt'\right). \tag{4}$$

This allows us the define an effective error Hamiltonian by switching into the interaction frame of the ideal gate

operation [41, 51, 52] (see also Appendix A)

$$H_{\text{error}} = U^{\dagger}_{\text{ideal}}(t) H U_{\text{ideal}}(t) - i\hbar U^{\dagger}_{\text{ideal}}(t)\dot{U}_{\text{ideal}}(t), \quad (5)$$

where $\dot{U}$ is the derivative of U with respect to time t. The effective error Hamiltonian now solely describes the erroneous operation and we can rewrite

$$\mathcal{E} = \mathcal{T}\exp\left(-\frac{i}{\hbar}\int_0^{t_g} H_{\text{error}}(t')dt'\right) \quad (6)$$

$$= \exp\left(\sum_{n=1}^{\infty}\bar{H}_n\right) \quad (7)$$

$$\approx \exp\left(-\frac{i}{\hbar}\int_0^{t_g} H_{\text{error}}(t')dt'\right). \quad (8)$$

From the first to the second line we applied the Magnus expansion with Magnus coefficients $\bar{H}_n$. We now make the standard assumptions such as small errors $||\mathcal{E} - \mathbb{1}|| \ll 1$ (otherwise choose a closer desired gate) to ensure a fast converging Magnus series. In the last step we truncated the Magnus expansion at lowest order. Numerical simulations show that this order is sufficient to achieve quantum operations with errors $1 - F < 10^{-4}$.

As a next step we now compute and investigate transition rates caused by the erroneous operation (error rates) $|\text{tr}(\mathcal{E}O)|^2$ where O is an operator of interest. The error rate $|\text{tr}(\mathcal{E}O)|^2$ is the probability to make a coherent error generated by $\mathcal{E}$ and "measured" by the operator O [53]. From this point a general treatment is not encouraged since to completely optimize the gate operation, $(n^2 - 1)$ transition rates need to be optimized simultaneously. Fortunately, for most systems of interest the interaction is sparse, e.g., interaction is localized or limited to neighboring qubits. In many cases single-qubit operators σ_x, σ_y, σ_z and two-qubit operators $\sigma_x\sigma_x$, $\sigma_y\sigma_y$, $\sigma_z\sigma_z$, where σ_i is the $i = x, y, z$ Pauli-matrix, are sufficient. For spin qubits typical targeted gate operations are $e^{i\phi\sigma_z}$ gates due to different qubit frequencies [12], $e^{i\phi\sigma_{x(y)}}$ single-qubit gates from resonant driving, and $e^{i\phi\sigma_z\sigma_z}$ two-qubit CPHASE gates. Under such sparse evolution the error rate typically takes the form (derivation see Appendix A)

$$|\text{tr}(\mathcal{E}O)|^2 \approx \left|\frac{1}{\hbar}\int_0^{t_g}\sum_n g_n(t)e^{if_n(t)/\hbar}dt\right|^2, \quad (9)$$

where $g_n(t)$ are functions connected with the erroneous evolution and $f_n(t)$ functions related to the desired evolution with each function depending on the choice of O. Without proof we now choose O such that there is only a single term in the sum involved (this is indeed the case for our targeted applications) and perform the substitution [46]

$$\dot{f}(t)dt = \hbar\nu_f t_g ds \quad (10)$$

with a constant ν_f. Under the implicit assumption $\dot{f}(t) \neq 0$ we arrive at the error rate

$$|\text{tr}(\mathcal{E}O)|^2 \approx \left|\frac{1}{\hbar}\int_{s(0)}^{s(t_g)}\tilde{g}(t(s))e^{i\nu_f t_g s}ds\right|^2, \quad (11)$$

$$= S(\tilde{g}(\nu_f t_g)), \quad (12)$$

with $\tilde{g}(t(s)) = g(t(s))\frac{dt}{ds}(s)$ and the energy spectral density S. In the first line we approximated $\sin(x) \approx x$ and from the first to the second line we replaced the integral which corresponds to a short-time Fourier transformation with the energy spectral power of an input signal [46]. As a consequence we have now shifted the task from minimizing the error rates to optimizing the energy spectral density, a task already investigated and in most cases solved. Conveniently, an experimental estimation of the error rates is much more efficient compared to the complex protocols required to compute the fidelity, since typically only a few expectation values are need to reconstruct the corresponding error rates.

Error mitigation strategies

1. Synchronization

We know (without proof) that Eq. (12) is an oscillatory function with respect to $\nu_f t_g$ due to the finite gate time t_g. This becomes clear by rewriting the short-time Fourier transformation as a convolution of the conventional Fourier transformation and the oscillating $\sin(x)/x$-function as the Fourier transform of the box function from the finite time interval $[0, t_g)$. Synchronization is the concept of finding minima of Eq. (12) which due to the oscillatory nature exist as shown in Fig. 1 (b). The optimal pulse length t_g or system parameter ν_f are then given by the minima of $S(\nu_f t_g)$. The concept of synchronization is best visualized in the special case of constant $\dot{f}(t)$ and $g(t)$ where even $S(\nu_f t_g) = 0$ is possible. These minima correspond to cases where the undesired interaction "undoes" itself, e.g. phase evolution for a SWAP gate [27] or off-resonant Rabi oscillations [44, 45]. An advantage of this strategy is the absence of any complex pulse shaping. However, the requirement for simultaneous minima in the spectrum makes it difficult to scale beyond a handful of qubits [45, 54]. Additionally, filtering in the signal transmission greatly reduce the effectiveness of the gate operations as seen in Fig. 1 (b).

2. Static pulse shaping

For purely real input signals, fast operations with consistently low error rates can be achieved using window functions $w(t)$ designed for optimized spectral concentration such as the discrete prolate spheroidal sequence (DPSS or Slepian), and the Dolph–Chebyshev window.

Alternatively, if faster operations at the cost of larger coherent errors are desired, a Hamming window is the best choice. The optimized window functions typically require a high computation cost, high bandwidth, and high time-resolution thus restricting their use. For many applications with limited bandwidth and low-pass filters, equally small errors can be achieved using approximations such as the Kaiser window [55]

$$w(t) = \mathcal{N}\mathcal{I}_0\left(\frac{2\lambda}{t_g}\sqrt{t(t_g-t)}\right) \tag{13}$$

with normalization constant $\mathcal{N}$ via $\int_0^{t_g} w(t)dt = t_g$ and $\mathcal{I}_0$ being the 0-th order modified Bessel function. Alternatively, one can also use the truncated Fourier expansions [46]

$$w(t) = w_{\text{even}}(t) + w_{\text{odd}}(t) \tag{14}$$

with the even and odd decomposition

$$w_{\text{even}}(t) = \sum_{n=1}^{N} \lambda_{\text{even},n}\left[1-\cos\left(\frac{2\pi n t}{t_g}\right)\right], \tag{15}$$

$$w_{\text{odd}}(t) = \sum_{n=1}^{N} \lambda_{\text{odd},n}\left[1-\sin\left(\frac{2\pi n t}{t_g}\right)\right]. \tag{16}$$

The coefficients $\lambda_{\text{even}} = [1.0715, -0.0795, 0.0043, 0.0037]$ and $\lambda_{\text{odd}} = [0,0,0,0]$ can be estimated from a Fourier decomposition of the slepian or from numerical minimization of the error rate [46]. By using only even components a smooth pulse-shape is guarantied. A simple and popular yet effective pulse shape is the Hann window ($\lambda_{\text{even}} = [1,0,0,0]$) that corresponds to a cosine shape. Another interesting pulse shape is the Tukey window defined as [31]

$$w(t,\lambda) = \begin{cases} \frac{1}{2-\lambda}\left[1-\cos\left(\frac{2\pi t}{\lambda t_g}\right)\right] & 0 \le t \le \frac{\lambda t_g}{2} \\ \frac{2}{2-\lambda} & \frac{\lambda t_g}{2} < t < t_g - \frac{\lambda t_g}{2} \\ \frac{1}{2-\lambda}\left[1-\cos\left(\frac{2\pi(t_g-t)}{\lambda t_g}\right)\right] & t_g - \frac{\lambda t_g}{2} \le t \le t_g \end{cases} \tag{17}$$

which consists of two ramps $w_{\text{even}}(t)$ with $\lambda_{\text{even}} = [1,0,0,0]$ interleaved by a constant part. The Tukey pulse has the advantage of having a lower peak amplitude compared to the non-interleaved pulse at the cost of steeper flanks. For $\lambda = 1$ it reduces to the Hann window. An interesting thought is also combining the Tukey window shape with the higher Fourier components which we will leave to the future.

The optimal pulse design is then given by setting

$$\tilde{g}(s) = Aw(t_g s) \tag{18}$$

with amplitude A being estimated from the desired operation (4). The relation between real time t and dilated normal time s is given by integrating Eq. (10) arriving at [46]

$$t(s) = \int_{s(0)=0}^{s} \frac{\hbar\nu_f t_g}{\dot{f}(s')}ds' \tag{19}$$

with $\hbar\nu_f t_g = f(t_g) - f(0)$. The inverted function is best acquired using numerical interpolation [46], e.g. `Mathematica` directly provides $\tilde{g}(t)$ using the command Interpolation[Table[$\{t[s], \tilde{g}[s]\}, \{s,0,1\}$]] with sufficient sampling. Fig. 1 (c) shows the resulting infidelity of a gate operation for different pulse shapes. As expectec the Kaiser window outperforms the conventional cosine shape.

3. *Dynamic pulse shaping*

For resonantly driven gates, i.e., single-qubit gates for spin qubits [12], the additional phase of the MW signal translates into complex $\tilde{g}(t(s)) = \tilde{g}_R(t(s)) + i\tilde{g}_I(t(s))$. Here, the real part $\tilde{g}_R(t(s))$ and imaginary part $\tilde{g}_I(t(s))$ correspond to the I/Q quadrature of the MW. This freedom can actively be used to further reduce the error rates compared to window functions [42], e.g., the derivative by removal of adiabatic gate (DRAG) [40, 56] and Wah-Wah [57–59] protocols both allow to greatly suppress crosstalk from off-resonant drives. This can be visualized by integrating Eq. (11) by parts with respect to the real part of the signal [60]

$$|\text{tr}(\mathcal{E}\,O|^2 = S\left(\frac{\frac{d}{ds}\tilde{g}_R(t(s))}{i\nu_f t_g} + i\tilde{g}_I(t(s))\right) \tag{20}$$

with boundary conditions $\tilde{g}_R(0) = \tilde{g}_R(t_g)$. We get a complete cancellation of the error rate with

$$\frac{\frac{d}{ds}\tilde{g}_R(t(s))}{\nu_f t_g} = \tilde{g}_I(t(s)), \tag{21}$$

where the pulse shape of $\tilde{g}_R(t(s))$ can individually be optimized using window functions. Fig. 1 (d) shows that using dynamic pulse shaping protocols (here DRAG) significantly reduces the error rate. For $\frac{dt}{ds} = \text{const}$ this exactly yields the DRAG condition $g_I \propto \dot{g}_R$. The advantage of this strategy is a very strong suppression of the error rate with the cost of additional power consumption which scales with the number of suppressed transitions [61]. Our framework allows to generalize this powerful method to all systems with independent control over two orthogonal axes.

III. APPLICATIONS

Before we apply our framework to optimize the performance of qubit operations we introduce a theoretical description of a spin qubit system. The dynamics in

the subsystem of two electron spins in the $(\cdots,1,1,\cdots)$ charge configuration of a multi-qubit network can be well-described by the Heisenberg model [26]

$$H = h\left(J\left(\boldsymbol{S}_1\cdot\boldsymbol{S}_2-\frac{1}{4}\right)+\boldsymbol{B}_1\cdot\boldsymbol{S}_1+\boldsymbol{B}_2\cdot\boldsymbol{S}_2\right) \tag{22}$$

with $\boldsymbol{S}_j = (\sigma_{x,j},\sigma_{y,j},\sigma_{z,j})^T/2$, where $\sigma_{k,j}$ is the Pauli-matrix acting on the spin in dot j and $\boldsymbol{B}_j = (B_{x,j},B_{y,j},B_{z,j})^T$ being the magnetic field felt by the the electron in dot j. For later convenience we define the average field $E_z = (B_{z,1}+B_{z,2})/2$ and the difference field $\Delta E_z = B_{z,2}-B_{z,1}$. Note that in this notation the magnetic field $\boldsymbol{B}$ and the exchange interaction J are in units of GHz.

Single-qubit gates are operated in the regime of negligible exchange interaction, $J\approx 0$, and implemented via resonant driving either via ESR or EDSR. Here, we do not distinguish between the two mechanisms and describe both by a static magnetic field $\boldsymbol{B}_{j,0}$ and an oscillating magnetic field $\boldsymbol{B}_{j,D}(t)$, such that $\boldsymbol{B}_j = \boldsymbol{B}_{j,0}+\boldsymbol{B}_{j,D}(t)$. We discuss here the case of two qubits driven by a single microwave tone.

Exchange-based two-qubit gates are operated in the regime of $J>0$. For simplicity, we assume that all two-qubit gates are operated deep inside the (1,1) charge occupation regime at the symmetric operation point and electric control is maintained via virtual barrier gates [10, 31, 62]. Theoretically, we describe the system using Hamiltonian (22) and move into a rotating frame $R=\exp[-i(2\pi\nu_D t+\theta)(S_1^z+S_2^z)]$ which leads in the standard basis $\{|\uparrow\uparrow\rangle, |\uparrow\downarrow\rangle, |\downarrow\uparrow\rangle, |\downarrow\downarrow\rangle\}$ to the following Hamiltonian [63]

$$H_{\mathrm{RF}} = \frac{h}{2}\begin{pmatrix} 2E_z-2\nu_D-\frac{\dot\theta}{2\pi} & B^*_{\perp,2}e^{-2\pi i\nu_D t} & B^*_{\perp,1}e^{-2\pi i\nu_D t} & 0 \\ B_{\perp,2}e^{2\pi i\nu_D t} & \Delta E_z - J & J & B^*_{\perp,1}e^{-2\pi i\nu_D t} \\ B_{\perp,1}e^{2\pi i\nu_D t} & J & -\Delta E_z - J & B^*_{\perp,2}e^{-2\pi i\nu_D t} \\ 0 & B_{\perp,1}e^{2\pi i\nu_D t} & B_{\perp,2}e^{2\pi i\nu_D t} & -(2E_z-2\nu_D-\frac{\dot\theta}{2\pi}) \end{pmatrix}, \tag{23}$$

where ν_D is the drive frequency, θ the phase of the drive, and $B_{\perp,j} = B_{x,j}+iB_{y,j}$ the perpendicular component of the magnetic field felt by qubit $j=1,2$ with respect to the quantization axis.

A. Resonant single-qubit gates

Expected coherent errors are crosstalk and other spectator errors from off-resonant drives [64], non-linear driving giving rise to higher harmonics and phase shifts [65], and frequency shifts from counter-rotating contributions (Bloch Siegert) [66]. To efficiently account for non-linear driving effects we expand the modulated (effective) magnetic field in terms of a Fourier series with respect to the drive frequency ν_D $\boldsymbol{B}_j(t) = \boldsymbol{\mathcal{B}}_{j,0}(t) + \sum_{k\neq 0}\boldsymbol{\mathcal{B}}_{j,k}(t)e^{-2\pi i\nu_D k t}$, where the Fourier components $\boldsymbol{\mathcal{B}}_0(t)$ and $\boldsymbol{\mathcal{B}}_k(t)$ are assumed to be slowly varying in the time interval $[0,\nu_D^{-1})$. The Hamiltonian can be significantly simplified under the rotating wave approximation (RWA) where we keep stationary terms and disregard all terms which are modulated with frequency $k\nu_D$ with $|k| = 1,2,3\cdots$. Corrections from violations of the rotating wave approximation (RWA) scale with $\Omega_{\mathrm{Rabi}}/\nu_D \sim 10^{-3}$ thus are most of the times negligible for typical experimental conditions but can become important for ultra-fast gate operations [67, 68] or driving at comparatively low frequencies [17]. In this section we focus on the RWA case and leave the latter to future investigations. We use the following Hamiltonian for our pulse optimization framework

$$H_{\mathrm{RWA}} = \frac{h}{2}\begin{pmatrix} 2(E_z-\nu_D)-\frac{\dot\theta}{2\pi} & (B^x_{2,1}-iB^y_{2,1})/2 & (B^x_{1,1}-iB^y_{1,1})/2 & 0 \\ (B^x_{2,-1}+iB^y_{2,-1})/2 & \Delta E_z & 0 & (B^x_{1,1}-iB^y_{1,1})/2 \\ (B^x_{1,-1}+iB^y_{1,-1})/2 & 0 & -\Delta E_z & (B^x_{2,1}-iB^y_{2,1})/2 \\ 0 & (B^x_{1,-1}+iB^y_{1,-1})/2 & (B^x_{2,-1}+iB^y_{2,-1})/2 & -2(E_z-\nu_D)+\frac{\dot\theta}{2\pi} \end{pmatrix}, \tag{24}$$

where we kept time-dependent phases to account for shifts in resonance frequency. Corrections beyond the RWA can be included by using directly Hamiltonian (23) instead or by applying the generalized RWA introduced in Ref. [69] and discussed in section III C.

Next we define the target operation as

$U_{\text{ideal}} = e^{-i\pi \int_0^t dt' [B^x_{1,1}(t') S^x_1 + 2(\Delta f(t') - \Delta E_z(t')) S^z_2]} e^{i\theta S^z_2}$ with frequency detuning $\Delta f(t) = E_z(t) + \frac{\Delta E_z(t)}{2} - \nu_D$ and find H_{error} via Eq. (5). Our target gate operation describes single-qubit Rabi oscillations and phase shifts on the non-driven qubit. The dominant effect of off-resonant driving, a phase accumulation (S^z_2) on the non-driven qubit known as ac-Stark shift, is included in the target operation to keep the erroneous evolution small since it can be corrected easily via virtual z gates. We identify two pairs of dominant error channels described by the operators $O_1 = S^z_1 \mp i S^y_1$ and $O_2 = S^x_2 \pm i S^y_2$ with erroneous evolutions

$$g_1(t) = \Delta f(t) - \frac{\dot{\theta}(t)}{2\pi} \mp i B^y_{1,1}(t), \tag{25}$$

$$g_2(t) = B^x_{2,1}(t) \pm i B^y_{2,1}(t), \tag{26}$$

desired evolutions

$$\dot{f}_1(t) = \pm \frac{h}{2} B^x_{1,1}(t), \tag{27}$$

$$\dot{f}_2(t) = \pm \frac{h}{2} \left(\Delta f(t') - \Delta E_z(t) - \frac{\dot{\theta}}{2\pi} \right) \tag{28}$$

and error rates

$$|\text{tr}(\mathcal{E} O_1)|^2 = S\big(\widetilde{g}_1[\nu_1 t_g]\big), \tag{29}$$

$$|\text{tr}(\mathcal{E} O_2)|^2 = S\big(\widetilde{g}_2[\nu_2 t_g]\big). \tag{30}$$

The first error rate describes a shift in the rotation axis (x-direction) of qubit 1 giving rise to S^y_1 and S^z_1 errors. The best mitigation strategy is dynamic pulse shaping via a time-dependent phase $\theta(t)$, e.g. through chirping [70, 71]. The second error rate describes a spin-flip of the second qubit due to off-resonant driving giving rise to S^x_2 and S^y_2 errors. The mitigation of the spin-flip errors requires either synchronization or pulse shaping.

The conditions for the synchronization of a $R_{x,y}(\pi)$ gate on qubit j affecting qubit i ($i \neq j$) with a rectangular pulse shape is (see also Ref. [45])

$$B^x_{i,1} = \frac{2n+1}{2m} \sqrt{\frac{(B^x_{j,1})^2}{4} + \Delta E_z^2} \tag{31}$$

with integer m and n. The condition for a synchronized $R_{x,y}(\frac{\pi}{2})$ gate is given by the substitution $n \to 2n$. For minimal gate time assuming an equally strong global drive $B^x_{i,1} = B^x_{j,1}$ the synchronization condition for a $R_x(\frac{\pi}{2})$ gate is simplified to

$$t_g = \frac{\sqrt{16m^2 - 1}}{4\Delta E_z} \tag{32}$$

which corresponds exactly to the minima in Fig. 1 (b).

For static pulse shaping, $\theta(t) = 0$ and $B^y_{i,j} = 0$, constant drive frequency $\nu_D = E_z \pm \Delta E_z$, and negligible shift in resonance frequency $\Delta E_z(t) = \Delta E_z$ the first error rate Eq. (29) vanishes and we only need to minimize Eq. (30) which is simplified to

$$|\text{tr}(\mathcal{E} O_2)|^2 = S\big(B^x_{2,1}[\Delta E_z t_g]\big). \tag{33}$$

Optimal pulse shapes for a $R_x(\frac{\pi}{2})$ gate are then given by $B^x_{2,1}(t) = \frac{1}{4} w(t)$, where we use the normalized window $\int_0^{t_g} w(t) dt = 1$. Fig. 1 (c) displays the simulated infidelity for different pulse shapes as a function of gate time t_g.

Under the same assumptions such as constant drive frequency $\nu_D = E_z \pm \Delta E_z$ and negligible shift in resonance frequency $\Delta E_z(t) = \Delta E_z$, dynamic pulse shaping provides even faster gate times with small errors (see Fig. 1) (c)-(d). Applying the DRAG method [40] Eqs. (29)-(30) combined with a cosine shape, the optimized dynamic pulse shape is (see Fig. 1 (d))

$$B^x_{2,1}(t) = \frac{1}{4} w(t) \left(1 - \frac{5}{5 + (4\Delta E_z t_g)^2} \right), \tag{34}$$

$$B^y_{2,1}(t) = -\frac{\dot{B}^x_{2,1}(t)}{\Delta E_z}, \tag{35}$$

$$\dot{\theta}(t) = -\frac{\left(\dot{B}^x_{2,1}(t)\right)^2}{\Delta E_z}. \tag{36}$$

The renormalization of the drive amplitude is due to the additional power in driving. The optimized pulse shape for driving qubit 2 is given by substituting $\Delta E_z \to -\Delta E_z$ in Eqs. (34)-(36).

B. Exchange-based two-qubit CZ gate

A crucial condition for high-fidelity two-qubit CZ gates is an adiabatic turn on/off or pulse of the exchange interaction, which can give rise to substantial errors if violated [31]. While in principle an echo pulse sequence allows to suppress non-adiabatic errors [44] for a CZ gate, the echo pulse is often inconvenient and introduces additional noise through the longer gate times.

Starting from Hamiltonian (23) we quickly notice that the exchange interaction only affects the odd parity states $\{|\uparrow\downarrow\rangle, |\downarrow\uparrow\rangle\}$ (see appendix B). Without loss of generality, this allows us to project the full dynamics on a two-level system taking into account the global phase of this subspace. Introducing a new set of Pauli operators $\sigma_x = |\uparrow\downarrow\rangle\langle\downarrow\uparrow| + |\downarrow\uparrow\rangle\langle\uparrow\downarrow|$, $\sigma_y = -i|\uparrow\downarrow\rangle\langle\downarrow\uparrow| + i|\downarrow\uparrow\rangle\langle\uparrow\downarrow|$, and $\sigma_z = |\uparrow\downarrow\rangle\langle\uparrow\downarrow| - |\downarrow\uparrow\rangle\langle\downarrow\uparrow|$, we find

$$H_{\text{sub}} = \frac{h}{2}\big(-J + \Delta E_z \, \sigma_z + J \, \sigma_x \big). \tag{37}$$

We define the ideal target operation as $U_{\text{ideal}} = e^{i\pi \int_0^t J(t') dt'} e^{-i\pi \int_0^t dt' \nu_{\text{j}}(t') \widetilde{\sigma}_z}$, where $\widetilde{\sigma}_{x,z} = U^\dagger_{\text{ST}} \sigma_{x,z} U_{\text{ST}}$ with eigenenergies $\nu_{\text{j}}(t) = \sqrt{\Delta E_z(t)^2 + J(t)^2}$ and unitary $U_{\text{ST}} = e^{-\frac{i}{2}\tan^{-1}\left(\frac{J(t)}{\Delta E_z(t)}\right)\sigma_y}$ diagonalizes Hamiltonian (37). Therefore, our target operations describes the adiabatic

phase evolution due to the exchange interaction. We identify a single dominant error channel described by the spin-flip operator $O = |\widetilde{\uparrow\downarrow}\rangle\langle\widetilde{\downarrow\uparrow}|$, where $|\widetilde{\uparrow\downarrow}\rangle$ and $|\widetilde{\downarrow\uparrow}\rangle$ are the eigenstates of Hamiltonian (37). The erroneous and targeted time evolutions are

$$g(t) = -h\frac{\Delta E_z\,\dot{J} - \Delta\dot{E}_z J}{4\pi\nu_{\rm j}^2}, \tag{38}$$

$$\dot{f}(t) = \frac{h}{2}\nu_{\rm j}. \tag{39}$$

For small exchange $J(t) \ll \Delta E_z$ and constant Zeeman splitting $\Delta E_z(t) \approx \Delta E_z$ we can simplify $g(t) \propto \dot{J}(t)$ and $\nu_j \approx \Delta E_z$ to find the error rate

$$P_{|\widetilde{\uparrow\downarrow}\rangle\to|\widetilde{\downarrow\uparrow}\rangle} \sim S\big(\dot{J}[\Delta E_z t_g]\big). \tag{40}$$

Remarkably, this optimization condition for an adiabatic CZ gate is identical to the condition for minimizing single-qubit crosstalk in Eq. (33) under the replacement $B^x_{2,1} \to \dot{J}$ with the same invariant $t_g\Delta E_z$. The conditions for the synchronization of a CZ gate with a rectangular pulse shape and minimal time t_g is [27]

$$t_g = \frac{\sqrt{4m^2-1}}{2\Delta E_z(v_B)} \tag{41}$$

with integer m. Here $\Delta E_z(v_B)$ is the difference in resonance frequency during the pulse. Note that this is equivalent to the synchronization condition of a $R_{x,y}(\pi)$ gate (see Eq. (32)).

While dynamic pulse shaping is not possible for a dc pulse (no two independent control axes which are orthogonal to each other) static pulse shaping is sufficient to get low error rates. Due to the non-linear relation between barrier voltage and exchange interaction (see Appendix B) the optimal pulse shape for the barrier voltage pulse shape $v_B(t)$ is then given by

$$v_B(t) = \frac{1}{\alpha}\log\left(\frac{\sqrt{J(t)/J_{\rm sat}}}{|1-J(t)/J_{\rm sat}|}\right), \tag{42}$$

$$J(s(t)) = \tan\left[2Aw(t_g s) + \tan^{-1}\left(\frac{J(0)}{\Delta E_z(0)}\right)\right]\Delta E_z, \tag{43}$$

$$\tag{44}$$

using the relation between real-time t and time s. The amplitude A is given by the conditional phase condition $\int_0^{t_g} J(t')dt' = 1/2$. For $J(t) \ll \Delta E_z$ and constant Zeeman splitting $\Delta E_z(t) \approx \Delta E_z$ we find

$$v_B(t) = \frac{1}{2\alpha}\log\left(\frac{w(t)}{2J_0 t_g} + 1\right), \tag{45}$$

where we use $t = t_g s$ and the normalized window $\int_0^{t_g} w(t)dt = t_g$.

C. Exchange-based two-qubit resonant SWAP gate

Another set of two-qubit gates can be accessed by driving the exchange interaction directly at the $|\widetilde{\uparrow\downarrow}\rangle \iff |\widetilde{\downarrow,\uparrow}\rangle$ resonance frequency $\nu_{\rm ST} = \sqrt{\Delta E_z^2 + J_0^2}$ [72, 73]. For the resonant SWAP gate, errors from violations of the rotating wave approximation due to $t_g \sim 100\,$ns compared to $\nu_{\rm ST} \sim 100\,$MHz and the influence of higher harmonics due to the non-linear voltage-exchange relation are no longer negligible. In general driving the barrier voltage $v_B(t) = v_{B,0} + v_{B,1}(t)\cos(2\pi\nu_{\rm ST}t + \theta_j)$ gives rise to

$$J(v_B) = \mathcal{J}_0(v_B) + \sum_{k>0} 2\mathcal{J}_k(v_B)\cos(2\pi\nu_{\rm ST}kt + k\theta), \tag{46}$$

$$\Delta E_z(v_B) = \Delta\mathcal{E}_{z,0}(v_B) + \sum_{k>0} 2\Delta\mathcal{E}_{z,k}(v_B)\cos(2\pi\nu_{\rm ST}kt + k\theta), \tag{47}$$

where we have expressed J and ΔE_z in terms of Fourier coefficients with respect to the drive frequency $\nu_{\rm ST}$. Since tuning the barrier voltage typically accompanies a change in resonance frequency [31], we consider this in our model $\Delta E_z \to \Delta E_z(v_B(t))$ with $\Delta E_z(v_{B,0}) = \Delta E_z$.

Without loss of generality, the dynamics is again projected on the odd-parity subspace spanned by $\{|\uparrow\downarrow\rangle, |\downarrow\uparrow\rangle\}$ and described by Hamiltonian (37). In order to simplify the Hamiltonian we perform a double basis transformation $U = e^{-i(\pi\nu_{\rm ST}t+\theta_j/2)\widetilde{\sigma}_z} e^{-\frac{i}{2}\tan^{-1}\left(\frac{J_0}{\Delta E_z}\right)\sigma_y}$ before we apply our framework. The first transformation diagonalizes $H_{\rm sub}(t=0)$ and the second moves us into the rotating frame with respect to the driving frequency and driving phase. The transformed and rotated Hamiltonian reads

$$\begin{aligned} H_{\rm ac} = &-\frac{h}{2}J(t) \\ &+ \frac{h}{2}\left(\frac{J_0\,J(t) + \Delta E_z\,\Delta E_z(t)}{\nu_{\rm ST}} - \nu_{\rm ST} - \frac{\dot{\theta}_j}{2\pi}\right)\widetilde{\sigma}_z \\ &+ \frac{h}{2}\left(\frac{\Delta E_z J(t) - J_0\Delta E_z(t)}{\nu_{\rm ST}} e^{2\pi i\nu_{\rm ST}t + i\theta_j}\right)\widetilde{\sigma}_+ + h.c. \end{aligned} \tag{48}$$

With this transformation, the target operation is simply expressed as $U_{\rm ideal} = e^{-i\pi\int_0^t dt'\cos(2\pi\nu_{\rm ST}t+\theta_j)(\Delta E_z J(t) - J_0\Delta E_z(t))\widetilde{\sigma}_x/\nu_{\rm j}(t)}$ which describes a flip between the eigenstates, i.e. $|0\rangle \sim |\uparrow\downarrow\rangle$ and $|1\rangle \sim |\downarrow\uparrow\rangle$ for $\Delta E_z \gg J_0$. We identify a single pair of error rates described by the operators $O = \widetilde{\sigma}_z \pm i\widetilde{\sigma}_y$. The erroneous and targeted time evolution

are

$$g(t) = \frac{J_0\, J(t) + \Delta E_z\, \Delta E_z(t)}{\nu_{\rm ST}} - \nu_{\rm ST} - \frac{\dot{\theta}_j}{2\pi} \mp i \sin(2\pi\nu_{\rm ST} t + \theta_j) \frac{\Delta E_z J(t) - J_0 \Delta E_z(t)}{2\nu_{\rm ST}}, \quad (49)$$

$$\dot{f}(t) = h \cos(2\pi\nu_{\rm ST} t + \theta_j) \frac{\Delta E_z J(t) - J_0 \Delta E_z(t)}{2\nu_{\rm ST}}. \quad (50)$$

a. General case In the general case no closed-form analytical expressions can be derived for Eq. (46) and one has to rely on numerical techniques. Additionally, static and dynamic pulse shaping is also not directly possible due to $g(t)$ being complex but can be made possible by focusing on the error rate. We start by separating $g(t) = g_R(t) + i g_I(t)$ where g_R and g_I are real functions and then perform integration by parts

$$|{\rm tr}(\mathcal{E}\, O)|^2 = \left| \int_0^{t_g} [g_R(t) + i g_I(t)] e^{if(t)/\hbar} dt \right|^2 \quad (51)$$

$$= \left| \int_0^{t_g} \left[g_R(t) + \frac{\dot{f}(t)}{\hbar} \int_0^t g_I(t') dt' \right] e^{if(t)/\hbar} dt \right|^2. \quad (52)$$

Here, we restrict ourselves to solutions where the limits of integration vanish at $t = 0, t_g$. Unfortunately, we cannot apply the next (optional) step of our framework and use the substitution (10) since $\dot{f} = 0$ gives rise to non-unique solutions. We note that our full framework can still be applied if we apply a (generalized) RWA [69] directly on Hamiltonian (48) to remove the oscillating components. Dynamic pulse shaping is however possible as we directly arrive at an integro-differential equation for the phase θ_j by plugging in Eqs. (49) and (50) whose solution provides an optimized $\theta_j(t)$.

b. Exponential exchange We will now consider the case of an exponential interaction $J(v_B) \propto e^{2\alpha v_B}$ and a linear frequency shifts, $\Delta E_z(v_B) = \Delta E_z + \beta\,(v_B - v_{B,0})$. This regime is experimentally accessed in Refs. [72, 73]. In this limit, exact analytic expressions can be derived since the Fourier coefficients are given by

$$\mathcal{J}_k(v_B) = J_0 \mathcal{I}_k(2\alpha(v_B - v_{B,0})) \quad (53)$$

for $k = 0, \pm 1$, where $\mathcal{I}_k$ denotes the modified Bessel function of order k. In this special case the optimized dynamic pulse shape can then be simplified to

$$v_{B,1}(t) = \frac{1}{2\alpha} \log\left(\frac{w(t)}{4 J_0 t_g} + 1 \right) \cos(2\pi\nu_{\rm ST} + \theta_j(t)) \quad (54)$$

with the dynamic phase

$$\theta_j(t) = 2\pi \int_0^t dt' \frac{J_0\, \mathcal{J}_0(v_B(t')) + \Delta E_z^2 - \nu_{\rm ST}^2}{\nu_{\rm ST}} + 2\pi \int_0^t dt' \frac{\Delta E_z J_1(t') - J_0 \beta\, v_{B,1}(t')}{\nu_{\rm ST}^2} \times \left[\frac{\Delta E_z J_0(t')}{2\pi\nu_{\rm ST}^3} + \frac{\Delta E_z J_1(t')}{4\pi\nu_{\rm ST}^3} - \frac{J_0 \beta\, v_{B,1}(t')}{8\pi\nu_{\rm ST}^3} - \sum_{k=2}^{\infty} \frac{\Delta E_z J_k(t')}{(k^2-1)\pi\nu_{\rm ST}^3} \right]. \quad (55)$$

The first term originates from the conventional RWA and compensates the shift in resonance frequency $h\sqrt{\Delta E_z^2 + J^2}$ due to non-linear exchange. The remaining term describes the driving-induced shift of the rotation angle and can be derived with the help of a generalized RWA [69] (see Appendix C).

IV. PERFORMANCE

In this section we show that the aforementioned techniques lead to high-fidelity single- and two-qubit gates. We benchmark the gates by computing the time-evolution of an input state $\Psi(t)$ by step-wise integration of the Schroedinger equation

$$i\hbar\dot{\Psi}(t) = H(t)\Psi(t), \quad (56)$$

where $H(t)$ is the exact Hamiltonian (23) in the rotating frame without neglecting the counter-rotating terms. Noise is added in two ways into the dynamics. Because of the slow dynamics compared to the gate times $< 1\,\mu$s, magnetic noise affecting the single spins is simulated by a quasi-static shift of the qubit resonance frequencies $B_{z,i}$. Charge noise is simulated using colored noise with a spectral density $S(f) = \frac{A^2}{2\pi f}$ using the Fourier Filter method [74, 75]. To simulate the performance at the symmetric operation point [10, 76], where decoherence is greatly improved, voltage fluctuations predominantly affect the exchange interaction non-linearly via the barrier potential $v_B(t) = v_{B,0}(t) + \delta v_B(t)$.

A. Resonant single-qubit gates

The most common gates in a multi-qubit algorithm are single-qubit gates. Therefore, each large-scale qubit device needs consistently small single-qubit error rates to fulfill the requirements for error correction [77, 78]. A frequently reported number are infidelities of $1 - F < 0.5 - 1\%$ for the physical gate operations [77, 79], although based on many assumption such as good initialization and readout and uncorrelated errors. Our simulations show that sufficiently small infidelities are within

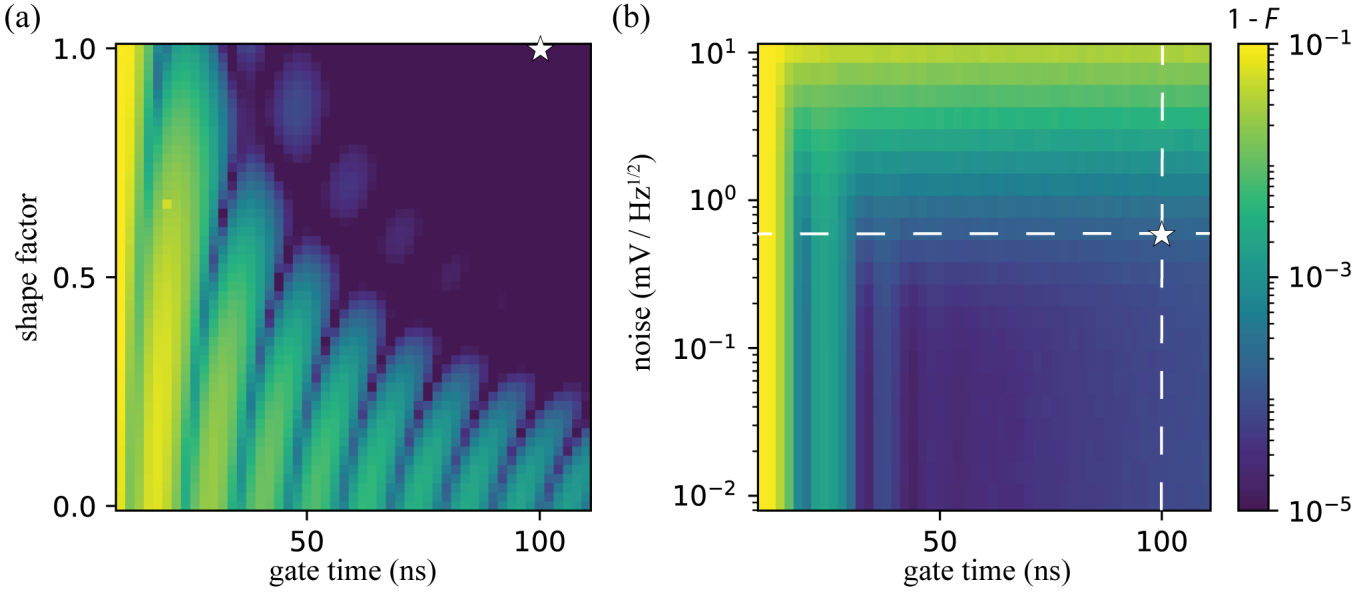

FIG. 2. (a) Simulated noiseless average gate infidelity $1-F$ for a CZ gate as a function of pulse length t_g and the shaping factor λ of the Tukey window Eq. (17). The star highlights the pulse shape used in Ref. [31] demonstrating $F = 99.6\,\%$ in isotopically enriched silicon quantum dots. (b) Simulated infidelity $1-F$ for a CZ gate as a function of pulse length t_g and charge noise amplitude A of the virtual voltage using a cosine shape ($\lambda = 1$). The dashed lines highlight the value of extracted charge noise and pulse duration from Ref. [31].

reach on state-of-the-art qubit devices using our framework. The simplest technique, synchronization of the Rabi-frequencies [44, 45] already shows extremely small infidelities in our simulations. However, low-pass filters in the signal transfer to limit high-frequency noise are a detrimental error source for the synchronization technique as seen in Fig. 1-(b) that shows the infidelity with (blue) and without (orange) a 150 MHz-Butterworth filter. The filter significantly reduces the dips as well as shifts the minima. On the other hand our simulations (see Fig. 1-(c)-(d)) show that high fidelity operations can still be reached using static or dynamic pulse shaping to reach infidelities as small as 10^{-4} for gate times in the order of $t_g = 25\,\text{ns}$ with a frequency separation of $|f_{Q,1} - f_{Q,2}| = 100\,\text{MHz}$. Note, that this on the one hand directly implies that gate times $t_g = 250\,\text{ns}$ are required if the frequency separation is reduced to $|f_{Q,1} - f_{Q,2}| = 10\,\text{MHz}$ as proposed in some architectures, e.g. Ref. [13], but on the other hand a larger frequency separation allows for faster high-fidelity gate operations [34, 80] due to the infidelity being invariant for $t_g \times |f_{Q,1} - f_{Q,2}|$. In the former case dynamic pulse shaping, such as the derivative removal by adiabatic gate (DRAG) protocol [40, 56] allows for an additional improvement.

B. Exchange-based two-qubit CZ gate

Many experiments on single-spin qubits use the universal CZ gate [27, 28] as their native high-fidelity two-qubit gate [19, 23, 31, 32, 34, 81] due to its simplicity and potential for scaling to larger arrays [25, 64]. The CZ gate

$$U_{\text{CZ}} = e^{-i\Phi_{\text{CZ}}\left(S_{1,z}S_{2,z} - \frac{1}{4}\right)} \tag{57}$$

$$\equiv \text{diag}(1, 1, 1, e^{i\Phi_{\text{CZ}}}) \tag{58}$$

with $\Phi_{\text{CZ}} = 2\pi \int_0^{t_g} J(t)dt$ can be directly acquired using only single-qubit phase gates [82] from the adiabatic phase evolution under the exchange interaction and can be transformed into a CNOT gate using two single-qubit $R_y(\frac{\pi}{2})$ gates. For the CZ gate the exchange interaction $J(t)$ is pulsed picking up a conditional phase $\Phi_{\text{CZ}} = (2n+1)\pi$ with integer n. Since the CZ gate is intended to be adiabatic by nature, it is also directly (linearly) susceptible to low-frequency noise acting on the resonance frequencies. However, we claim that a substantial error in previous realizations [19, 83] is due to violations of the adiabaticity condition which is more severely impacted due to the non-linear voltage-exchange relation and gives rise to bit-flip errors. Here, the adiabaticity condition is with respect to the frequency difference $|f_{Q,2} - f_{Q,1}|$ between the two spin qubits. Since the coherent errors of a CZ two-qubit and resonant single-qubit gates are related and $t_g \times |f_{Q,1} - f_{Q,2}|$ is an invariant in the simulations, we know that the CZ gate can, for example, be further improved using the Kaiser window or increasing the sep-

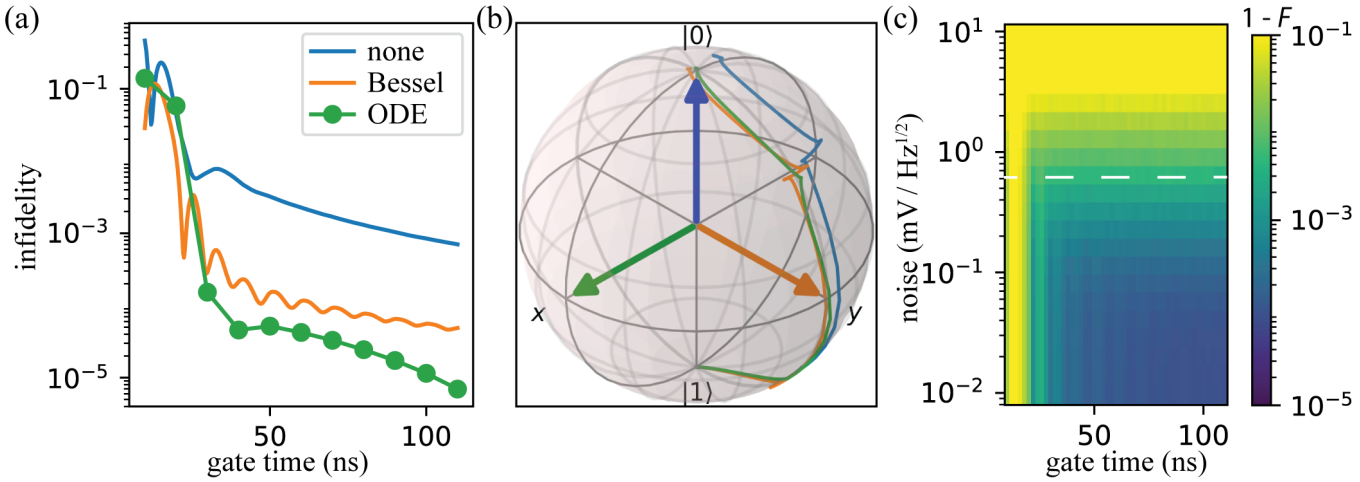

FIG. 3. (a) Simulated average gate infidelity $1-F$ of a SWAP-class gate as a function of pulse length t_g using no dynamic pulse shaping (blue), dynamic pulse shaping based on Bessel functions Eq. (55) (orange), and dynamic pulse shaping based on a ODE approximation of Eq. (52) (green). The simulation using ODE was performed with Mathematica. (b) Trajectories of the optimized pulse shapes for a $t_g = 40\,\text{ns}$ projected on the Bloch sphere. Only dynamic pulse shaping based on the ODE approximation gives rise to a high fidelity state flip. (c) Simulated gate infidelity $1-F$ as a function of pulse length t_g and charge noise amplitude A of the virtual voltage using a cosine shape and dynamic pulse shaping based on Bessel functions. The dashed line highlights the value of charge noise of the virtual voltage extracted in Ref. [31].

aration in qubit frequency. Fig. 2 (a) shows the simulated infidelity of a CZ gate as a function of gate time t_g and the proportionality factor $\alpha \in [0,1]$ from the Tukey window, see Eq. (17). The oscillating infidelity as a function of exchange corresponds to an interference pattern of the diabatic contributions identical to the one observed in Fig. 1 (b) and (c). On the other hand a small frequency separation severely limits the performance since long gate times $t_g = 300\,\text{ns}$ are required if the frequency separation is reduced to $|f_{Q,1} - f_{Q,2}| = 10\,\text{MHz}$ [84, 85]. In situations with a small frequency separation splitting a non-adiabatic CZ gate can be realized as shown theoretically [27] and demonstrated experimentally [83] using the synchronization condition. Our simulations confirm such high-fidelity gates in Fig. 2 (a) for $\lambda = 0$, where the Tukey pulse corresponds to a rectangular pulse. However, the diabatic implementation requires a precise timing, is sensitive to pulse imperfections such as filter effects, and is prone to dephasing due to low-frequency noise.

We now compare our results to recent experiments demonstrating high-fidelity CZ-gate operations with infidelities $1-F = 4\times10^{-3}$ [31] and $1-F = 2\times10^{-3}$ [34]. Both experiments are performed in isotopically enriched silicon quantum dots which are prone to (low-frequency) charge noise. Low-frequency noise couples to the CZ-gate through the diagonal matrix elements $S^z_{1,(2)}$ and $S^z_1 S^z_2$ via the qubit frequencies ΔE_z and via the exchange interaction J. In Fig. 2 we highlighted the pulse shape, expected noise level, and pulse duration (star) of the extracted parameters in Ref. [31]. Our simulation predicts coherent errors as low as $1-F = 10^{-5}$ and total errors of $1-F = 2\times10^{-4}$ are achievable. We speculate that the discrepancy of simulations and experiment is related to heating effects [65]. While we haven't performed simulations using the parameters in Ref. [34] we can nevertheless predict the coherent infidelity using the invariant $t_g \times |f_{Q,1} - f_{Q,2}|$. The conversion results in a rectangular pulse with an effective gate duration $\widetilde{t}_g = 158\,\text{ns}$ due to the frequency difference $|f_{Q,2} - f_{Q,1}| = 396\,\text{MHz}$ (derivation see appendix F for details). Our simulations predict a coherent infidelity of $1-F = 5\times10^{-4}$ which is increased to $1-F = 8\times10^{-4}$ if incoherent noise sources are included.

Fig. 2 (b) shows the CZ gate infidelity in general as a function of charge noise amplitude A and gate time t_g showing the importance of the interplay between coherent and incoherent errors. Too fast gates suffer from coherent errors while too slow gates are prone to incoherent errors with an optimum depending on the charge noise amplitude. Taking into account realistic values [31] (see dashed line in Fig. 2) (b)) one can clearly observe that coherent errors from non-adiabicity are dominating for $t_g < 40\,\text{ns}$ and infidelities as low as $1-F = 10^{-4}$ are possible.

C. Exchange-based two-qubit resonant SWAP gates

While arbitrary single-qubit gates combined with CZ form a universal gate set for quantum circuits, it is often more efficient to include additional gates into the gate set. A frequently neccessary gate in qubit architectures with next-neighbor couplings only is the SWAP gate, as

it enables long-range qubit-qubit communication as well as read-out [13, 64, 72, 73]. The SWAP-class gate

$$U_{\text{SWAP}}(\phi) = \begin{pmatrix} 1 & 0 & 0 & 0 \\ 0 & 0 & e^{i\Phi_{\text{SWAP}}} & 0 \\ 0 & e^{i\Phi_{\text{SWAP}}} & 0 & 0 \\ 0 & 0 & 0 & 1 \end{pmatrix}. \tag{59}$$

can be either accessed directly through a diabatic exchange pulse for small frequency differences $|f_{Q,2} - f_{Q,1}| \ll J$ [28, 83] or in general by driving the exchange interaction at the frequency difference $|f_{Q,2} - f_{Q,1}|$ between the corresponding qubits. Here we defined the SWAP-class gate via the additional phase $\Phi_{\text{SWAP}} = \pi \int_0^{t_g} J(t)dt$. For $\Phi_{\text{SWAP}} = n\pi$ we recover the classical swap-gate while the iSWAP, $\Phi_{\text{SWAP}} = (2n+1)\pi/2$, maximally entangles the qubits during the swap. Fig. 3 (a) shows the simulated infidelity of a SWAP-class gate for different static and dynamic pulse shapes assuming perfect phase compensation. Due to the non-linear exchange interaction and short target gate times $|f_{Q,2} - f_{Q,1}| \sim 1/t_g$ dynamic pulse shaping greatly enhances the performance of the gates. For situations when the explicit phase Φ_{SWAP} matters, e.g., compiling Clifford gates using iSWAP gate, we provide two methods. The simplest method to obtain for example a iSWAP gate is to append a CZ gate such that $\Phi_{\text{SWAP}} + \Phi_{\text{CZ}}/2 = (2n+1)\pi/2$ [72]. Remarkably, one can also perform the compensation CZ gate simultaneously with the SWAP gate by combining an ac and dc control signal. This has the advantage of a faster gate time at the cost of additional calibrations.

The SWAP-class is directly (linear) susceptible to low-frequency noise coupling in via the exchange interaction J. Additionally, both discussed implementations have in common that they require careful calibration to compensate for the adiabatic phase acquisition from exchange making them (at least) equally susceptible to low-frequency charge noise as the conventional CZ gate. Fig. 4 compares the infidelity of the different two-qubit gate implementations discussed in this paper. It is clearly visible that the CZ gate always outperforms the SWAP-class gate. The lower fidelity of the SWAP gate is due to the overall larger conditional phase picked up, $\Phi_{\text{SWAP}} \approx 2\Phi_{\text{PHASE}}$.

D. Conclusion

In this work we have presented a framework which allows us to characterize unitary errors and how to suppress these for various basic gate operations for spin qubits. Unitary errors mostly arise due to violations of approximations such as the rotating wave approximation, larger system sizes in the form of crosstalk, and through non-linear transfer functions of the input signal. Our numerical simulations show that for state-of-the-art experiments unitary errors can indeed be the limiting factor.

Explicitly, we used our framework to obtain optimized pulse shapes for a resonantly driven single-qubit gates and exchange-based dc or ac gates on single-spin qubits. These techniques have been successfully implemented and enabled a two-qubit CZ gate with fidelity $F = 99.6$ [31]. We have also shown that the optimized static pulse shapes for single-qubit gates and CZ two-qubit gates are identical and only depend on the qubit frequency separation. This possibly allows for a direct on-chip integration of the control electronics with little memory requirements. The transformation of the signal to compensate the exponential relationship between voltage and exchange interaction is possible using efficient digital algorithms or an analog logarithmic element.

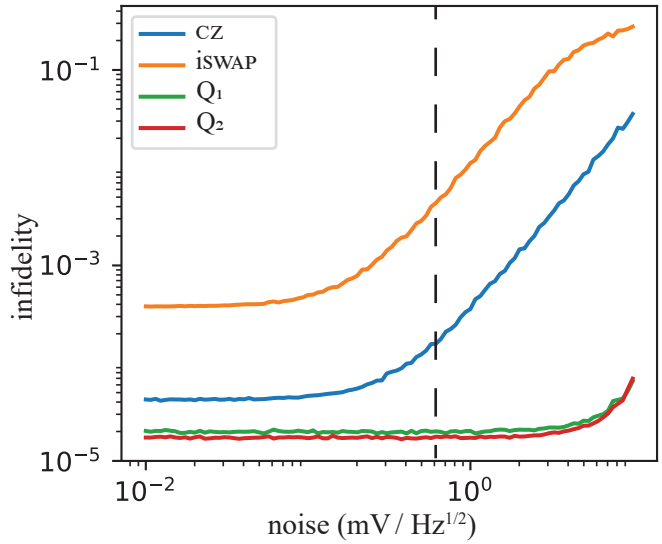

FIG. 4. Simulated infidelity $1 - F$ of the CZ gate, iSWAP gate, and single-qubit $R_{x,1}(\pi/2)$ gates on qubit Q_1 and Q_2 as a function of charge noise amplitude σ_{v_B} of the virtual voltage with a constant level of nuclear noise. All gate times are $t_g = 35\,\text{ns}$. The dashed line highlights the value of charge noise of the virtual voltage extracted in Ref. [31].

Our framework and also all of the presented optimized pulse shapes are directly applicable to different platforms. To suppress coherent errors even further, higher-order Magnus expansion terms can be taken into account [41]. In our formalism this would correspond to not only minimizing the spectral density but also minimizing higher correlations such as the bi-spectrum or multi-spectrum.

While in this work we focused on improving the performance of operations with respect to coherent errors we see no issue with expanding the formalism to also account for incoherent errors. We can think of two steps how this can be achieved. First, we can either extend our formalism to describing the time dynamics in terms of a propagator based on the Liouville superoperator instead of unitary operations [53]. Alternatively, to account for low-frequency noise, we can combine our framework with the geometric gate formalism introduced in Ref. [86].

ACKNOWLEDGMENTS

The authors greatly acknowledge the contributions of S. de Snoo to the manuscript. We thank all members of the Veldhorst and Vandersypen group, M. Mehmandoost, D. Zeuch, V. Evangelos, and Vincent Bejach for inspiring and helpful discussion. M.R. acknowledges support from NWO under Veni grant (VI.Veni.212.223). This research was sponsored by the Army Research Office (ARO) under grant numbers W911NF-17-1-0274 and W911NF-12-1-0607. The views and conclusions contained in this document are those of the authors and should not be interpreted as representing the official policies, either expressed or implied, of the ARO or the US Government. The US Government is authorized to reproduce and distribute reprints for government purposes notwithstanding any copyright notation herein.

DATA AVAILABILITY

Simulation software and data analysis scripts supporting this publication are available at doi: 10.5281/zenodo.7341187.

Appendix A: Sparse time evolution

Starting from Eq. (8) we now derive Eq. (9) which is the starting point of our framework. We do this in two steps. First, the interior form of Eq. (9) is a direct consequence of the separation of the dynamics into desired and erroneous Hamiltonian contributions, $H = H_{\text{ideal}} + H_{\text{rest}}$, combined with the transformation into the interaction frame with respect to H_{ideal} due to $i\hbar U^\dagger_{\text{ideal}}(t)\dot{U}_{\text{ideal}}(t) = H_{\text{ideal}}$. Thus we can rewrite Eq. (5)

$$\begin{aligned} H_{\text{error}} &= U^\dagger_{\text{ideal}}(t) H U_{\text{ideal}}(t) - i\hbar U^\dagger_{\text{ideal}}(t)\dot{U}_{\text{ideal}}(t), && \text{(A1)}\\ &= U^\dagger_{\text{ideal}}(t) H U_{\text{ideal}}(t) - H_{\text{ideal}}, && \text{(A2)}\\ &= U^\dagger_{\text{ideal}}(t)(H_{\text{ideal}} + H_{\text{rest}})U_{\text{ideal}}(t) - H_{\text{ideal}}, && \text{(A3)}\\ &= U^\dagger_{\text{ideal}}(t) H_{\text{rest}} U_{\text{ideal}}(t) \\ &\quad + U^\dagger_{\text{ideal}}(t) H_{\text{ideal}} U_{\text{ideal}}(t) - H_{\text{ideal}}, && \text{(A4)}\\ &= U^\dagger_{\text{ideal}}(t) H_{\text{rest}} U_{\text{ideal}}(t), && \text{(A5)} \end{aligned}$$

where we only inserted the two upper definitions and the commutativity between H_{ideal} and U_{ideal}. In the next step we separate $H_{\text{rest}} = H_{\text{rest,c}} + H_{\text{rest,a}}$, where $H_{\text{rest,c}}$ is the commuting component $[H_{\text{rest,c}}, U_{\text{ideal}}(t)] = 0$ and $H_{\text{rest,a}}$ the remainder. The commuting component can be corrected independently of the ideal operation thus trivially calibrated or corrected. Without loss of generality we assume $H_{\text{rest,c}} = 0$ otherwise we redefine $H_{\text{ideal}} = H_{\text{ideal}} + H_{\text{rest,c}}$ and drop the sub-indices. We can now always define a set of complex parameters $g_k(f_k)$ associated to the erroneous (ideal) dynamics to rewrite every matrix element of

$$H_{\text{error},k_1,k_2} = \sum_k g_k(t) e^{i f_k(t)/\hbar} \tag{A6}$$

as no restrictions are placed on g_k and f_k. Second, the outer form of Eq. (9) follows directly from the lowest-order Magnus expansion. Since we assumed small errors we truncate the matrix exponential (Eq. (8)) in linear order

$$\begin{aligned} \mathcal{E} &\approx \exp\left(-\frac{i}{\hbar}\int_0^{t_g} H_{\text{error}}(t')dt'\right) && \text{(A7)}\\ &\approx 1 + \left(-\frac{i}{\hbar}\int_0^{t_g} H_{\text{error}}(t')dt'\right) && \text{(A8)} \end{aligned}$$

Without loss of generality, we now choose the operator $O = |k_1\rangle\langle k_2|$ since otherwise we can rewrite $O = \sum_m O_m$, restrict ourselves to a single operator component O_m, and sum up the components afterwards. Finally, combining Eq. (A6) and Eq. (A8) gives rise to the final expression Eq. (9) in the main text. An alternative derivation of Eq. (9) for a specific application case using a geometric interpretation can be found in Ref. [46].

Appendix B: Modeling the exchange interaction

Eq. (22) of the main text is an approximation of the spin-dynamics in the low-energy subspace considering a single fermion in the left and right quantum dots, $(1,1)$ charge configuration, in the presence of small spin-orbit interaction [87, 88]. The origin of the spin-orbit interaction (SOI) may arise from intrinsic properties [89] or artificial created through the deployment of micromagnets [90]. Without (with negligible) SOI the low-energy dynamics of the spin can be derived starting from a Hubbard model with spin-conserving tunneling elements using a Schrieffer-Wolff approximation. Due to the Pauli exclusion principle, the spin state of a doubly occupied orbital state is always a spin singlet. Therefore, in the $(1,1)$ configuration only the singlet state, $|S\rangle = \frac{1}{\sqrt{2}}(|\uparrow\downarrow\rangle - |\downarrow\uparrow\rangle)$, can hybridize and be lowered in energy. Consequently, the exchange interaction can be written as

$$\begin{aligned} H_{\text{exchange}} &= -hJ\,|S\rangle\langle S| && \text{(B1)}\\ &= hJ\,(\boldsymbol{S}_1\cdot\boldsymbol{S}_2 - \frac{1}{4}). && \text{(B2)} \end{aligned}$$

The dynamics of the (isotropic) exchange interaction is thus limited to the singlet-state. In the presence of a difference in qubit resonance frequencies ΔE_z the $|\uparrow\downarrow\rangle$ and $|\downarrow\uparrow\rangle$ states are energetically separated, thus coupling the singlet with the triplet $|T_0\rangle = \frac{1}{\sqrt{2}}(|\uparrow\downarrow\rangle + |\downarrow\uparrow\rangle)$ state.

The amplitude of the exchange interaction J is a non-linear function of an applied (virtual) barrier voltage

v_B. In most experiments the exchange interaction can be modelled as an exponential function [91–93]

$$J(v_B) = J_{\text{sat}} e^{2\alpha(v_B - v_{\text{off}})} \tag{B3}$$

$$\equiv J_0 e^{2\alpha v_B}. \tag{B4}$$

Other experiments [10, 30], further indicate a saturation for large exchange values, thus, the upper expression (B4) can be seen as an approximation for $J \ll J_{\text{sat}}$. A more general expression considering saturation reads [10]

$$J(v_B) = J_{\text{sat}} \left(\sqrt{1 + e^{-2\alpha(v_B - v_{\text{off}})}} - e^{-\alpha(v_B - v_{\text{off}})} \right)^2. \tag{B5}$$

Here α is the leverarm, v_{off} is an offset which is set by the residual exchange interaction $J_{\text{res}} = J(0)$, and J_{sat} describes the saturation value of the exchange interaction when the two electrons are strongly hybridized. In practice J_{sat} can be motivated to be the singlet-triplet splitting or exchange splitting for a merged double quantum dot.

The presence of a valley degree of freedom [94, 95] affects the exchange interaction J as well as the frequency difference ΔE_z. In lowest-order perturbation theory we find

$$\Delta \widetilde{E}_z = \Delta E_z \left[1 - \left(\frac{t^2}{U^2} + \frac{2t^2}{(E_{V,1} + E_{V,2} + 2U)^2} \right) \right], \tag{B6}$$

$$\widetilde{J} = J \, \frac{1 + \cos(\phi_{V,1} - \phi_{V,2})}{2}, \tag{B7}$$

where $E_{V,i}$ and $\phi_{V,i}$ are the respective valley splitting and valley phase of dot i. Plugging in realistic parameters $t = 20\,\mu\text{eV}$, $U = 3\,\text{meV}$, $\Delta E_z = 100\,\text{MHz}$, and $E_V = 200\,\mu\text{eV}$ we find $\Delta E_z - \Delta \widetilde{E}_z \approx 8\,\text{kHz}$. On contrast a finite valley phase difference significantly suppresses the exchange interaction [96]. For our theoretical simulations the valley phase becomes only problematic once it changes during the pulse, e.g. due to the deformation of the wave-functions as a function of applied voltages. Since the dc and ac pulsed two-qubit gates are adiabatic with respect to the qubit frequencies $f_{Q,1,Q,2} = E_z \pm \Delta E_z/2$ and in most devices also with respect to the valley splitting E_V the gates are only slightly affected by the presence of an excited valley degree. This latter case requires microscopic computations which are not part of this paper, therefore, we assume a constant valley phase difference which we factor out. A last remark, both correction factors are unimportant in an experimental realization for the here discussed gates since this renormalization is already accounted for during the calibration process of the the qubit energy difference and the spin exchange strength.

In the presence of spin-orbit interaction, spin non-conserving tunneling is allowed which gives rise to an isotropic exchange interaction [25, 97]

$$H_{\text{exchange,anisotropic}} = h \boldsymbol{S}_1 \mathcal{J} \boldsymbol{S}_2, \tag{B8}$$

where $\mathcal{J}$ is the exchange tensor. Therefore, the dynamics of the exchange interaction is no longer limited to the $\{|S\rangle, |T_0\rangle\}$ subspace. Additionally, in the presence of SOI the quantization axis of the spins in the different quantum dots may change thus giving rise to an additional channel that can couple the $|T_0\rangle$ state with the polarized $|T_+\rangle = |\uparrow,\uparrow\rangle$ and $|T_-\rangle = |\downarrow,\downarrow\rangle$ states. Note, that this situation may also arise for electron systems with micromagnets designed to enhance SOI [98, 99]. However, most results from this paper can still be applied to platforms with small to medium strength SOI, such as planar electron qubits in silicon and hole qubits [16], as long as a sufficiently strong external magnetic field is applied to suppress to unwanted dynamics.

Appendix C: Generalized rotating wave approximation

In our framework we now apply an "exact" rotating wave approximation described in Ref. [69]. Although other approaches based either on the Magnus expansion [100] or Floquet engineering [101] or numerical methods [102] allow to find control pulses for a strongly driven qubit system we find the exact RWA to be most intuitive to incorporate in non-linear situations. The effective Hamiltonian is then given by [69]

$$\begin{aligned} H_{\text{effective}} = \; & \nu_D \int_0^{\nu_D^{-1}} dt' H_{\text{RF}}(t') \\ & + \nu_D \int_0^{\nu_D^{-1}} dt' \dot{H}_{\text{RF}}(t') t' \\ & + \frac{\nu_D}{2\hbar i} \int_0^{\nu_D^{-1}} dt' \int_0^{t'} dt'' [H_{\text{RF}}(t'), H_{\text{RF}}(t'')] \\ & + \mathcal{O}\left(\frac{1}{\nu_D}\right)^2, \end{aligned} \tag{C1}$$

where $[A, B] = AB - BA$ denotes the commutator and $\dot{A} = \frac{d}{dt} A$ is the time derivative. An important remark is, that H_{RF} and $\dot{H}_{\text{RF}}$ are assumed to be either constant or periodic in the time interval $[0, \nu_D^{-1})$. The first line in Eq. (C1) is the conventional rotating wave approximation. The second line addresses corrections due to the time-dependence of signals such as envelopes of the applied signals. The last line includes the first order corrections of the rotating wave approximation such as the Bloch-Sigert shift.

Appendix D: Approximating the integro-differential equation using a ordinary differential equation

Writing out Eq. (52) we find the integro-differential equation

$$\frac{\dot{\theta}_j(t)}{4\pi} = \frac{2\pi}{2\nu_{ST}^2}\left[(\Delta E_z J(t)\cos(2\pi\nu_{ST}t+\theta_j(t)) - J_0\Delta E_z(t)\cos(2\pi\nu_{ST}t+\theta_j(t))\right] \times\left(\int_0^t (\Delta E_z J(s)\sin(2\pi\nu_{ST}s+\theta_j(s)) - J_0\Delta E_z(s)\sin(2\pi\nu_{ST}s+\theta_j(s)))\,ds\right) + \frac{\Delta E_z\Delta E_z(t) + J_0 J(t) - \nu_{ST}^2}{2\nu_{ST}}. \tag{D1}$$

The upper system is generally hard to solve, thus we approximate the upper expression using a series expansions in $\theta_j(t)$ at $\theta_j(0)$ up to first order. To arrive at an ordinary differential equation (ODE) we additionally ignore all terms under the integral which depend on θ_j. A numerical check confirmed the validity assuming reasonable smooth pulse shapes.

Appendix E: Master equation solver

For all numerical simulations performed we solve the time-dependent Schrödinger equation

$$i\hbar\frac{d}{dt}\left|\psi(t)\right\rangle = H\left|\psi(t)\right\rangle \tag{E1}$$

and compute the unitary propagator iterative according to

$$U(t+\Delta t) = e^{-\frac{i}{\hbar}H(t+\Delta t)}U(t). \tag{E2}$$

Here, $H(t+\Delta t)$ is discretized into N segments of length Δt such that $H(t)$ is constant in the time-interval $[t, t+\Delta t)$. For the simulations of single-qubit gates in Figs. 1 (b)-(d) we choose an external magnetic field $E_z = 10\,\text{GHz}$ and a step-size of $\Delta t = 0.2\,\text{ps}$. The remaining simulations involving two-qubit gates in Figs. 2 and 3 are performed in the rotating frame of the external magnetic field E_z and neglecting the counter-rotating terms, the so-called rotating wave approximation (RWA). This allows us to chose the time-step $\Delta t = 10\,\text{ps}$ being sufficiently small. For each simulation we check whether the RWA holds.

In all our simulations except for ODE 3 (a) (green) to emulate the realistic effect of a finite band-with and filtering of the control gates we add on each input signal, amplitude and phase of barrier voltage and drive voltage, a low-pass filter with a cut-off frequency of 150 MHz. In particular we use a butterworth filter of order 3 implemented via the Scipy package [103].

For our noisy simulations we included classical fluctuations of the matrix elements of the Hamiltonian

$$H(t,\boldsymbol{\beta}(t)) \to H(t,\boldsymbol{\beta}(t)+\delta\boldsymbol{\beta}(t)), \tag{E3}$$

where $\boldsymbol{\beta}(t)$ are parameters describing the dynamics of the system and $\delta\boldsymbol{\beta}(t)$ are the fluctuations of the parameter. We note, that this treatment allows us to account for non-linear Hamiltonian interactions as the exchange interaction and also to include 'sweet spots', points of operation where the first order dynamics vanishes. The fluctuations $\delta\beta_j(t)$ are described by its spectral density $S_{\delta\beta_j}(w) = \int_{-\infty}^{\infty}\left(\int_{-\infty}^{\infty}\delta\beta_j(t)\delta\beta_j(t-t')dt'\right)e^{-iwt}dt$ which we use as input in our simulations. To compute time-traces of the fluctuation we use the Fourier filtering method [74, 75] to generate time-correlated time traces obeying $S_{\delta\beta_j}(w)$. In this method N independent Gaussian distributed numbers are generated and associated to a segment with time Δt. We then perform a discrete Fourier transformation, apply a frequency filter $\sqrt{S_{\delta\beta_j}(\Delta w)}$, and perform an inverse Fourier transformation. The resulting fluctuations are discretized in N segments with time Δt such that $\delta\beta_j(t)$ is constant in the time interval $[t, t+\Delta t)$. Note, that the same Δt is used as above. Consequently, fluctuations which are faster than $f_{\max} = \frac{1}{\Delta t}$ are truncated. The lower frequency cut-off of the discretized noise traces is given by the length of the simulation and the number of segments. In order to provide better comparison of the dynamics of unequal length simulations and avoid an increase of simulations length we add static fluctuations β_{static} to compensate for the 'missing' low-frequency components. The amount of static noise component is given by

$$\text{Var}(\beta_{\text{j,static}}) = \frac{1}{\pi}\int_{2\pi f_{\min}}^{\frac{2\pi}{t_{\text{sim}}}} S_{\delta\beta_j}(w)d\omega, \tag{E4}$$

where t_{sim} is the length of the simulation and $f_{\min} = 0.1\,\text{Hz}$ is a lower-frequency cut-off and resembles the retuning cycle of an experiment.

The final superoperator of the noisy process is then constructed as follows

$$\chi = \frac{1}{N_j}\sum_j U_{\text{j}}^\dagger(t_g)\otimes U_{\text{j}}(t_g), \tag{E5}$$

where $U_j(t=t_g)$ is the final unitary time evolution operator for a noise realization j and $N_j = 5000$ is the total number of noise realizations.

Appendix F: of coherent CZ gate error in Mills. et al.

We find the following device parameter in Ref. [34] describing the CZ gate; difference in qubit resonance frequency $\Delta\widetilde{E}_z = 396\,\text{MHz}$, duration of CZ gate $t_g = 40\,\text{ns}$

using a (smoothed) rectangular pulse shape (Tukey window with $\lambda \approx 0$). From Eq. 40 we know that the CZ error probability only depends on $\Delta E_z t_g$. This invariant allows us to conveniently simulate the coherent error using $\Delta E_z = 100\,\mathrm{MHz}$ (as for all other simulations in this manuscript) but using a modified pulse time $\widetilde{t_g} = t_g \times \Delta\widetilde{E}_z/\Delta E_z = 158.4\,\mathrm{ns}$. For the noisy simulations we used the same noise strength as extracted from Ref. [31] (as for all other simulations in this manuscript). We argue that the longer gate time (thus more noise) is compensated by the faster dephasing observed in Ref. [34].

[1] R. Hanson, L. P. Kouwenhoven, J. R. Petta, S. Tarucha, and L. M. K. Vandersypen, Spins in few-electron quantum dots, Rev. Mod. Phys. **79**, 1217 (2007).

[2] A. Morello, J. J. Pla, F. A. Zwanenburg, K. W. Chan, K. Y. Tan, H. Huebl, M. Mottonen, C. D. Nugroho, C. Yang, J. A. van Donkelaar, A. D. C. Alves, D. N. Jamieson, C. C. Escott, L. C. L. Hollenberg, R. G. Clark, and A. S. Dzurak, Single-shot readout of an electron spin in silicon, Nature (London) **467**, 687 (2010).

[3] B. M. Maune, M. G. Borselli, B. Huang, T. D. Ladd, P. W. Deelman, K. S. Holabird, A. A. Kiselev, I. Alvarado-Rodriguez, R. S. Ross, A. E. Schmitz, M. Sokolich, C. A. Watson, M. F. Gyure, and A. T. Hunter, Coherent singlet-triplet oscillations in a silicon-based double quantum dot, Nature (London) **481**, 344 (2012).

[4] J. J. Pla, K. Y. Tan, J. P. Dehollain, W. H. Lim, J. J. L. Morton, D. N. Jamieson, A. S. Dzurak, and A. Morello, A single-atom electron spin qubit in silicon, Nature (London) **489**, 541 (2012).

[5] C. H. Yang, W. H. Lim, N. S. Lai, A. Rossi, A. Morello, and A. S. Dzurak, Orbital and valley state spectra of a few-electron silicon quantum dot, Phys. Rev. B **86**, 115319 (2012).

[6] E. Kawakami, P. Scarlino, D. R. Ward, F. R. Braakman, D. E. Savage, M. G. Lagally, M. Friesen, S. N. Coppersmith, M. A. Eriksson, and L. M. K. Vandersypen, Electrical control of a long-lived spin qubit in a Si/SiGe quantum dot, Nat. Nanotechnol. **9**, 666 (2014).

[7] J. T. Muhonen, J. P. Dehollain, A. Laucht, F. E. Hudson, R. Kalra, T. Sekiguchi, K. M. Itoh, D. N. Jamieson, J. C. McCallum, A. S. Dzurak, and A. Morello, Storing quantum information for 30 seconds in a nanoelectronic device, Nat. Nanotechnol. **9**, 986 (2014).

[8] M. Veldhorst, J. C. C. Hwang, C. H. Yang, A. W. Leenstra, B. de Ronde, J. P. Dehollain, J. T. Muhonen, F. E. Hudson, K. M. Itoh, A. Morello, and A. S. Dzurak, An addressable quantum dot qubit with fault-tolerant control-fidelity, Nat. Nanotechnol. **9**, 981 (2014).

[9] K. Eng, T. D. Ladd, A. Smith, M. G. Borselli, A. A. Kiselev, B. H. Fong, K. S. Holabird, T. M. Hazard, B. Huang, P. W. Deelman, I. Milosavljevic, A. E. Schmitz, R. S. Ross, M. F. Gyure, and A. T. Hunter, Isotopically enhanced triple-quantum-dot qubit, Sci. Adv. **1**, e1500214 (2015).

[10] M. D. Reed, B. M. Maune, R. W. Andrews, M. G. Borselli, K. Eng, M. P. Jura, A. A. Kiselev, T. D. Ladd, S. T. Merkel, I. Milosavljevic, E. J. Pritchett, M. T. Rakher, R. S. Ross, A. E. Schmitz, A. Smith, J. A. Wright, M. F. Gyure, and A. T. Hunter, Reduced Sensitivity to Charge Noise in Semiconductor Spin Qubits via Symmetric Operation, Phys. Rev. Lett. **116**, 110402 (2016).

[11] W. I. L. Lawrie, N. W. Hendrickx, F. van Riggelen, M. Russ, L. Petit, A. Sammak, G. Scappucci, and M. Veldhorst, Spin Relaxation Benchmarks and Individual Qubit Addressability for Holes in Quantum Dots, Nano Letters **20**, 7237 (2020).

[12] G. Burkard, T. D. Ladd, J. M. Nichol, A. Pan, and J. R. Petta, Semiconductor Spin Qubits, arXiv:2112.08863 10.48550/arXiv.2112.08863 (2021).

[13] L. M. K. Vandersypen, H. Bluhm, J. S. Clarke, A. S. Dzurak, R. Ishihara, A. Morello, D. J. Reilly, L. R. Schreiber, and M. Veldhorst, Interfacing spin qubits in quantum dots and donors—hot, dense, and coherent, npj Quantum Information **3**, 1 (2017).

[14] M. Veldhorst, H. G. J. Eenink, C. H. Yang, and A. S. Dzurak, Silicon CMOS architecture for a spin-based quantum computer, Nature Communications **8**, 1766 (2017).

[15] F. A. Zwanenburg, A. S. Dzurak, A. Morello, M. Y. Simmons, L. C. L. Hollenberg, G. Klimeck, S. Rogge, S. N. Coppersmith, and M. A. Eriksson, Silicon quantum electronics, Rev. Mod. Phys. **85**, 961 (2013).

[16] G. Scappucci, C. Kloeffel, F. A. Zwanenburg, D. Loss, M. Myronov, J.-J. Zhang, S. De Franceschi, G. Katsaros, and M. Veldhorst, The germanium quantum information route, Nature Reviews Materials , 1 (2020).

[17] F. H. L. Koppens, C. Buizert, K. J. Tielrooij, I. T. Vink, K. C. Nowack, T. Meunier, L. P. Kouwenhoven, and L. M. K. Vandersypen, Driven coherent oscillations of a single electron spin in a quantum dot, Nature (London) **442**, 766 (2006).

[18] J. P. Dehollain, J. T. Muhonen, R. Blume-Kohout, K. M. Rudinger, J. K. Gamble, E. Nielsen, A. Laucht, S. Simmons, R. Kalra, A. S. Dzurak, and A. Morello, Optimization of a solid-state electron spin qubit using gate set tomography, New Journal of Physics **18**, 103018 (2016).

[19] M. Veldhorst, C. H. Yang, J. C. C. Hwang, W. Huang, J. P. Dehollain, J. T. Muhonen, S. Simmons, A. Laucht, F. E. Hudson, K. M. Itoh, A. Morello, and A. S. Dzurak, A two-qubit logic gate in silicon, Nature (London) **526**, 410 (2015).

[20] K. C. Nowack, F. H. L. Koppens, Y. V. Nazarov, and L. M. K. Vandersypen, Coherent Control of a Single Electron Spin with Electric Fields, Science **318**, 1430 (2007).

[21] J. Yoneda, K. Takeda, T. Otsuka, T. Nakajima, M. R. Delbecq, G. Allison, T. Honda, T. Kodera, S. Oda, Y. Hoshi, N. Usami, K. M. Itoh, and S. Tarucha, A quantum-dot spin qubit with coherence limited by charge noise and fidelity higher than 99.9%, Nat. Nanotechnol. **13**, 102 (2018).

[22] D. M. Zajac, A. J. Sigillito, M. Russ, F. Borjans, J. M. Taylor, G. Burkard, and J. R. Petta, Resonantly driven

CNOT gate for electron spins, Science **359**, 439 (2018).
[23] T. F. Watson, S. G. J. Philips, E. Kawakami, D. R. Ward, P. Scarlino, M. Veldhorst, D. E. Savage, M. G. Lagally, M. Friesen, S. N. Coppersmith, M. A. Eriksson, and L. M. K. Vandersypen, A programmable two-qubit quantum processor in silicon, Nature (London) **555**, 633 (2018).
[24] N. W. Hendrickx, D. P. Franke, A. Sammak, G. Scappucci, and M. Veldhorst, Fast two-qubit logic with holes in germanium, Nature **577**, 487 (2020).
[25] N. W. Hendrickx, W. I. L. Lawrie, M. Russ, F. van Riggelen, S. L. de Snoo, R. N. Schouten, A. Sammak, G. Scappucci, and M. Veldhorst, A four-qubit germanium quantum processor, Nature **591**, 580 (2021).
[26] D. Loss and D. P. DiVincenzo, Quantum computation with quantum dots, Phys. Rev. A **57**, 120 (1998).
[27] G. Burkard, D. Loss, D. P. DiVincenzo, and J. A. Smolin, Physical optimization of quantum error correction circuits, Phys. Rev. B **60**, 11404 (1999).
[28] T. Meunier, V. E. Calado, and L. M. K. Vandersypen, Efficient controlled-phase gate for single-spin qubits in quantum dots, Phys. Rev. B **83**, 121403 (2011).
[29] J. R. Petta, A. C. Johnson, J. M. Taylor, E. A. Laird, A. Yacoby, M. D. Lukin, C. M. Marcus, M. P. Hanson, and A. C. Gossard, Coherent Manipulation of Coupled Electron Spins in Semiconductor Quantum Dots, Science **309**, 2180 (2005).
[30] O. E. Dial, M. D. Shulman, S. P. Harvey, H. Bluhm, V. Umansky, and A. Yacoby, Charge Noise Spectroscopy Using Coherent Exchange Oscillations in a Singlet-Triplet Qubit, Physical Review Letters **110**, 146804 (2013).
[31] X. Xue, M. Russ, N. Samkharadze, B. Undseth, A. Sammak, G. Scappucci, and L. M. K. Vandersypen, Quantum logic with spin qubits crossing the surface code threshold, Nature **601**, 343 (2022).
[32] M. T. Mądzik, S. Asaad, A. Youssry, B. Joecker, K. M. Rudinger, E. Nielsen, K. C. Young, T. J. Proctor, A. D. Baczewski, A. Laucht, V. Schmitt, F. E. Hudson, K. M. Itoh, A. M. Jakob, B. C. Johnson, D. N. Jamieson, A. S. Dzurak, C. Ferrie, R. Blume-Kohout, and A. Morello, Precision tomography of a three-qubit donor quantum processor in silicon, Nature **601**, 348 (2022).
[33] A. Noiri, K. Takeda, T. Nakajima, T. Kobayashi, A. Sammak, G. Scappucci, and S. Tarucha, Fast universal quantum gate above the fault-tolerance threshold in silicon, Nature **601**, 338 (2022).
[34] A. R. Mills, C. R. Guinn, M. J. Gullans, A. J. Sigillito, M. M. Feldman, E. Nielsen, and J. R. Petta, Two-qubit silicon quantum processor with operation fidelity exceeding 99%, Science Advances **8**, eabn5130 (2022).
[35] S. J. Glaser, U. Boscain, T. Calarco, C. P. Koch, W. Köckenberger, R. Kosloff, I. Kuprov, B. Luy, S. Schirmer, T. Schulte-Herbrüggen, D. Sugny, and F. K. Wilhelm, Training Schrödinger's cat: Quantum optimal control, The European Physical Journal D **69**, 279 (2015).
[36] L. S. Pontryagin, *Mathematical Theory of Optimal Processes: Mathematical Theory of Optimal Processes L.s. Pontryagin Selected Works Volume 4*, Classics of Soviet Mathematics (Harwood Academic, Amsterdam, Netherlands, 1987).
[37] N. Khaneja, T. Reiss, C. Kehlet, T. Schulte-Herbrüggen, and S. J. Glaser, Optimal control of coupled spin dynamics: Design of NMR pulse sequences by gradient ascent algorithms, Journal of Magnetic Resonance **172**, 296 (2005).
[38] T. Caneva, T. Calarco, and S. Montangero, Chopped random-basis quantum optimization, Physical Review A **84**, 022326 (2011).
[39] K. Bergmann, H. Theuer, and B. W. Shore, Coherent population transfer among quantum states of atoms and molecules, Reviews of Modern Physics **70**, 1003 (1998).
[40] F. Motzoi, J. M. Gambetta, P. Rebentrost, and F. K. Wilhelm, Simple Pulses for Elimination of Leakage in Weakly Nonlinear Qubits, Physical Review Letters **103**, 110501 (2009).
[41] H. Ribeiro, A. Baksic, and A. A. Clerk, Systematic Magnus-Based Approach for Suppressing Leakage and Nonadiabatic Errors in Quantum Dynamics, Physical Review X **7**, 011021 (2017).
[42] L. S. Theis, F. Motzoi, S. Machnes, and F. K. Wilhelm, Counteracting systems of diabaticities using DRAG controls: The status after 10 years (a), EPL (Europhysics Letters) **123**, 60001 (2018).
[43] Throughout the paper fidelity always refer to the average gate fidelity.
[44] M. Russ, D. M. Zajac, A. J. Sigillito, F. Borjans, J. M. Taylor, J. R. Petta, and G. Burkard, High-fidelity quantum gates in Si/SiGe double quantum dots, Phys. Rev. B **97**, 085421 (2018).
[45] I. Heinz and G. Burkard, Crosstalk analysis for single-qubit and two-qubit gates in spin qubit arrays, Physical Review B **104**, 045420 (2021).
[46] J. M. Martinis and M. R. Geller, Fast adiabatic qubit gates using only σ_z control, Physical Review A **90**, 022307 (2014).
[47] M. Nielsen and I. Chuang, *Quantum Computation and Quantum Information*, Cambridge Series on Information and the Natural Sciences (Cambridge Univ. Press, 2002).
[48] E. Magesan, J. M. Gambetta, and J. Emerson, Characterizing quantum gates via randomized benchmarking, Physical Review A **85**, 042311 (2012).
[49] S. Aaronson, Shadow Tomography of Quantum States, SIAM Journal on Computing **49**, STOC18 (2020).
[50] E. Nielsen, J. K. Gamble, K. Rudinger, T. Scholten, K. Young, and R. Blume-Kohout, Gate Set Tomography, Quantum **5**, 557 (2021).
[51] A. Messiah, *Quantum Mechanics* (North-Holland, Amsterdam, 1961).
[52] A. Brinkmann, Introduction to average Hamiltonian theory. I. Basics, Concepts in Magnetic Resonance Part A **45A**, e21414 (2016).
[53] R. Blume-Kohout, M. P. da Silva, E. Nielsen, T. Proctor, K. Rudinger, M. Sarovar, and K. Young, A Taxonomy of Small Markovian Errors, PRX Quantum **3**, 020335 (2022).
[54] M. J. Gullans and J. R. Petta, Protocol for a resonantly driven three-qubit toffoli gate with silicon spin qubits, Phys. Rev. B **100**, 085419 (2019).
[55] F. F. Kuo and J. F. Kaiser, *System Analysis by Digital Computer* (Wiley, New York, 1967).
[56] E. Lucero, J. Kelly, R. C. Bialczak, M. Lenander, M. Mariantoni, M. Neeley, A. D. O'Connell, D. Sank, H. Wang, M. Weides, J. Wenner, T. Yamamoto, A. N. Cleland, and J. M. Martinis, Reduced phase error through optimized control of a superconducting qubit,

Physical Review A **82**, 042339 (2010).
[57] R. Schutjens, F. A. Dagga, D. J. Egger, and F. K. Wilhelm, Single-qubit gates in frequency-crowded transmon systems, Physical Review A **88**, 052330 (2013).
[58] V. Vesterinen, O.-P. Saira, A. Bruno, and L. DiCarlo, Mitigating information leakage in a crowded spectrum of weakly anharmonic qubits, arXiv:1405.0450 10.48550/arXiv.1405.0450 (2014).
[59] L. S. Theis, F. Motzoi, and F. K. Wilhelm, Simultaneous gates in frequency-crowded multilevel systems using fast, robust, analytic control shapes, Physical Review A **93**, 012324 (2016).
[60] F. Motzoi, J. M. Gambetta, S. T. Merkel, and F. K. Wilhelm, Optimal control methods for rapidly time-varying Hamiltonians, Physical Review A **84**, 022307 (2011).
[61] J. M. Gambetta, F. Motzoi, S. T. Merkel, and F. K. Wilhelm, Analytic control methods for high-fidelity unitary operations in a weakly nonlinear oscillator, Physical Review A **83**, 012308 (2011).
[62] F. K. Malinowski, F. Martins, P. D. Nissen, S. Fallahi, G. C. Gardner, M. J. Manfra, C. M. Marcus, and F. Kuemmeth, Symmetric operation of the resonant exchange qubit, Phys. Rev. B **96**, 045443 (2017).
[63] Here and below we use the notation that $|\downarrow\rangle$ and $|\uparrow\rangle$ correspond to ground and excited qubit state.
[64] S. G. J. Philips, M. T. Mądzik, S. V. Amitonov, S. L. de Snoo, M. Russ, N. Kalhor, C. Volk, W. I. L. Lawrie, D. Brousse, L. Tryputen, B. P. Wuetz, A. Sammak, M. Veldhorst, G. Scappucci, and L. M. K. Vandersypen, Universal control of a six-qubit quantum processor in silicon, Nature **609**, 919 (2022).
[65] B. Undseth, X. Xue, M. Mehmandoost, M. Russ, N. Samkharadze, A. Sammak, V. V. Dobrovitski, G. Scappucci, and L. M. K. Vandersypen, Nonlinear response and crosstalk of strongly driven silicon spin qubits, arXiv:2205.04905 10.48550/arXiv.2205.04905 (2022).
[66] J. Romhányi, G. Burkard, and A. Pályi, Subharmonic transitions and Bloch-Siegert shift in electrically driven spin resonance, Phys. Rev. B **92**, 054422 (2015).
[67] F. N. M. Froning, L. C. Camenzind, O. A. H. van der Molen, A. Li, E. P. A. M. Bakkers, D. M. Zumbühl, and F. R. Braakman, Ultrafast hole spin qubit with gate-tunable spin–orbit switch functionality, Nature Nanotechnology **16**, 308 (2021).
[68] K. Wang, G. Xu, F. Gao, H. Liu, R.-L. Ma, X. Zhang, Z. Wang, G. Cao, T. Wang, J.-J. Zhang, D. Culcer, X. Hu, H.-W. Jiang, H.-O. Li, G.-C. Guo, and G.-P. Guo, Ultrafast coherent control of a hole spin qubit in a germanium quantum dot, Nature Communications **13**, 206 (2022).
[69] D. Zeuch, F. Hassler, J. J. Slim, and D. P. DiVincenzo, Exact rotating wave approximation, Annals of Physics **423**, 168327 (2020).
[70] L. M. K. Vandersypen and I. L. Chuang, NMR techniques for quantum control and computation, Rev. Mod. Phys. **76**, 1037 (2005).
[71] M. Shafiei, K. C. Nowack, C. Reichl, W. Wegscheider, and L. M. K. Vandersypen, Resolving spin-orbit- and hyperfine-mediated electric dipole spin resonance in a quantum dot, Phys. Rev. Lett. **110**, 107601 (2013).
[72] A. J. Sigillito, M. J. Gullans, L. F. Edge, M. Borselli, and J. R. Petta, Coherent transfer of quantum information in a silicon double quantum dot using resonant SWAP gates, npj Quantum Information **5**, 1 (2019).
[73] F. van Riggelen, W. I. L. Lawrie, M. Russ, N. W. Hendrickx, A. Sammak, M. Rispler, B. M. Terhal, G. Scappucci, and M. Veldhorst, Phase flip code with semiconductor spin qubits, npj Quantum Information **8**, 1 (2022).
[74] Y.-C. Yang, S. N. Coppersmith, and M. Friesen, Achieving high-fidelity single-qubit gates in a strongly driven charge qubit with 1/f charge noise, npj Quantum Information **5**, 12 (2019).
[75] J. V. Koski, A. J. Landig, M. Russ, J. C. Abadillo-Uriel, P. Scarlino, B. Kratochwil, C. Reichl, W. Wegscheider, G. Burkard, M. Friesen, S. N. Coppersmith, A. Wallraff, K. Ensslin, and T. Ihn, Strong photon coupling to the quadrupole moment of an electron in a solid-state qubit, Nature Physics **16**, 642 (2020).
[76] F. Martins, F. K. Malinowski, P. D. Nissen, E. Barnes, S. Fallahi, G. C. Gardner, M. J. Manfra, C. M. Marcus, and F. Kuemmeth, Noise Suppression Using Symmetric Exchange Gates in Spin Qubits, Phys. Rev. Lett. **116**, 116801 (2016).
[77] R. Raussendorf and J. Harrington, Fault-Tolerant Quantum Computation with High Threshold in Two Dimensions, Physical Review Letters **98**, 190504 (2007).
[78] D. Lidar and T. Brun, *Quantum Error Correction* (2013).
[79] A. G. Fowler, M. Mariantoni, J. M. Martinis, and A. N. Cleland, Surface codes: Towards practical large-scale quantum computation, Phys. Rev. A **86**, 032324 (2012).
[80] W. I. L. Lawrie, M. Russ, F. van Riggelen, N. W. Hendrickx, S. L. de Snoo, A. Sammak, G. Scappucci, and M. Veldhorst, Simultaneous driving of semiconductor spin qubits at the fault-tolerant threshold, arXiv:2109.07837 10.48550/arXiv.2109.07837 (2021).
[81] X. Xue, T. F. Watson, J. Helsen, D. R. Ward, D. E. Savage, M. G. Lagally, S. N. Coppersmith, M. A. Eriksson, S. Wehner, and L. M. K. Vandersypen, Benchmarking Gate Fidelities in a Si/SiGe Two-Qubit Device, Phys. Rev. X **9**, 021011 (2019).
[82] Can be implemented virtually using only software phase shifts.
[83] L. Petit, M. Russ, G. H. G. J. Eenink, W. I. L. Lawrie, J. S. Clarke, L. M. K. Vandersypen, and M. Veldhorst, Design and integration of single-qubit rotations and two-qubit gates in silicon above one Kelvin, Communications Materials **3**, 1 (2022).
[84] L. Petit, H. G. J. Eenink, M. Russ, W. I. L. Lawrie, N. W. Hendrickx, S. G. J. Philips, J. S. Clarke, L. M. K. Vandersypen, and M. Veldhorst, Universal quantum logic in hot silicon qubits, Nature **580**, 355 (2020).
[85] C. H. Yang, R. C. C. Leon, J. C. C. Hwang, A. Saraiva, T. Tanttu, W. Huang, J. Camirand Lemyre, K. W. Chan, K. Y. Tan, F. E. Hudson, K. M. Itoh, A. Morello, M. Pioro-Ladrière, A. Laucht, and A. S. Dzurak, Operation of a silicon quantum processor unit cell above one kelvin, Nature **580**, 350 (2020).
[86] E. Barnes, F. A. Calderon-Vargas, W. Dong, B. Li, J. Zeng, and F. Zhuang, Dynamically corrected gates from geometric space curves, Quantum Science and Technology **7**, 023001 (2022).
[87] G. Burkard, D. Loss, and D. P. DiVincenzo, Coupled quantum dots as quantum gates, Phys. Rev. B **59**, 2070 (1999).

[88] X. Hu and S. Das Sarma, Hilbert-space structure of a solid-state quantum computer: Two-electron states of a double-quantum-dot artificial molecule, Physical Review A **61**, 062301 (2000).

[89] R. Winkler, *Spin-Orbit Coupling Effects in Two-Dimensional Electron and Hole Systems (Springer Tracts in Modern Physics)* (2003).

[90] Y. Tokura, W. G. van der Wiel, T. Obata, and S. Tarucha, Coherent Single Electron Spin Control in a Slanting Zeeman Field, Phys. Rev. Lett. **96**, 047202 (2006).

[91] P. Cerfontaine, R. Otten, M. A. Wolfe, P. Bethke, and H. Bluhm, High-fidelity gate set for exchange-coupled singlet-triplet qubits, Physical Review B **101**, 155311 (2020).

[92] C. J. van Diepen, P. T. Eendebak, B. T. Buijtendorp, U. Mukhopadhyay, T. Fujita, C. Reichl, W. Wegscheider, and L. M. K. Vandersypen, Automated tuning of inter-dot tunnel coupling in double quantum dots, Applied Physics Letters **113**, 033101 (2018).

[93] A. Pan, T. E. Keating, M. F. Gyure, E. J. Pritchett, S. Quinn, R. S. Ross, T. D. Ladd, and J. Kerckhoff, Resonant exchange operation in triple-quantum-dot qubits for spin–photon transduction, Quantum Science and Technology **5**, 034005 (2020).

[94] N. Rohling and G. Burkard, Universal quantum computing with spin and valley states, New Journal of Physics **14**, 083008 (2012).

[95] A. David, G. Burkard, and A. Kormányos, Effective theory of monolayer TMDC double quantum dots, 2D Materials **5**, 035031 (2018).

[96] B. Tariq and X. Hu, Impact of the valley orbit coupling on exchange gate for spin qubits in silicon, npj Quantum Information **8**, 1 (2022).

[97] B. Hetényi, C. Kloeffel, and D. Loss, Exchange interaction of hole-spin qubits in double quantum dots in highly anisotropic semiconductors, Physical Review Research **2**, 033036 (2020).

[98] X. Mi, M. Benito, S. Putz, D. M. Zajac, J. M. Taylor, G. Burkard, and J. R. Petta, A coherent spin-photon interface in silicon, Nature **555**, 599 (2018).

[99] N. Samkharadze, G. Zheng, N. Kalhor, D. Brousse, A. Sammak, U. C. Mendes, A. Blais, G. Scappucci, and L. M. K. Vandersypen, Strong spin-photon coupling in silicon, Science **359**, 1123 (2018).

[100] T. Figueiredo Roque, A. A. Clerk, and H. Ribeiro, Engineering fast high-fidelity quantum operations with constrained interactions, npj Quantum Information **7**, 1 (2021).

[101] C. Deng, F. Shen, S. Ashhab, and A. Lupascu, Dynamics of a two-level system under strong driving: Quantum-gate optimization based on Floquet theory, Physical Review A **94**, 032323 (2016).

[102] S. Safaei, S. Montangero, F. Taddei, and R. Fazio, Optimized single-qubit gates for Josephson phase qubits, Physical Review B **79**, 064524 (2009).

[103] P. Virtanen, R. Gommers, T. E. Oliphant, M. Haberland, T. Reddy, D. Cournapeau, E. Burovski, P. Peterson, W. Weckesser, J. Bright, S. J. van der Walt, M. Brett, J. Wilson, K. J. Millman, N. Mayorov, A. R. J. Nelson, E. Jones, R. Kern, E. Larson, C. J. Carey, İ. Polat, Y. Feng, E. W. Moore, J. VanderPlas, D. Laxalde, J. Perktold, R. Cimrman, I. Henriksen, E. A. Quintero, C. R. Harris, A. M. Archibald, A. H. Ribeiro, F. Pedregosa, P. van Mulbregt, and SciPy 1.0 Contributors, SciPy 1.0: Fundamental Algorithms for Scientific Computing in Python, Nature Methods **17**, 261 (2020).